PHYSICAL REVIEW D

PARTICLES AND FIELDS

THIRD SERIES, VOLUME 31, NUMBER 9 1 MAY 1985

Inclusive hadron production in upsilon decays and in nonresonant electron-positron annihilation at 10.49 GeV

S. Behrends, K. Chadwick, T. Gentile, Jan M. Guida, Joan A. Guida, A. C. Melissinos, S. L. Olsen, G. Parkhurst, R. Poling, C. Rosenfeld, E. H. Thorndike, and P. Tipton
University of Rochester, Rochester, New York 14627

D. Besson, J. Green, R. Namjoshi, F. Sannes, P. Skubic,* A. Snyder,† and R. Stone
Rutgers University, New Brunswick, New Jersey 08854

A. Chen, M. Goldberg, N. Horwitz, A. Jawahery, P. Lipari, G. C. Moneti, C. G. Trahern, and H. van Hecke
Syracuse University, Syracuse, New York 13210

S. E. Csorna, L. Garren, M. D. Mestayer, R. S. Panvini, and Xia Yi
Vanderbilt University, Nashville, Tennessee 37235

M. S. Alam
State University of New York at Albany, Albany, New York 12222

P. Avery, C. Bebek, K. Berkelman, D. G. Cassel, J. W. DeWire, R. Ehrlich, T. Ferguson, R. Galik, M. G. D. Gilchriese, B. Gittelman, M. Halling, D. L. Hartill, S. Holzner, M. Ito, J. Kandaswamy, D. L. Kreinick, Y. Kubota, N. B. Mistry, F. Morrow, E. Nordberg, M. Ogg, D. Peterson, K. Read, A. Silverman, P. C. Stein, S. Stone, and Xu Kezun
Cornell University, Ithaca, New York 14853

A. J. Sadoff
Ithaca College, Ithaca, New York 14850

R. T. Giles, J. Hassard, M. Hempstead, K. Kinoshita, W. W. MacKay,‡ F. M. Pipkin, and Richard Wilson
Harvard University, Cambridge, Massachusetts 02138

P. Haas, T. Jensen, H. Kagan, and R. Kass
Ohio State University, Columbus, Ohio 43210
(Received 18 October 1984)

We report measurements of single-particle inclusive spectra and two-particle correlations in decays of the $\Upsilon(1S)$ resonance and in nonresonant annihilations of electrons and positrons at center-of-mass energy 10.49 GeV, just below $B\bar{B}$ threshold. These data were obtained using the CLEO detector at the Cornell Electron Storage Ring (CESR) and provide information on the production of π, K, ρ, K^*, ϕ, p, Λ, and Ξ in quark and gluon jets. The average multiplicity of hadrons per event for upsilon decays (compared with continuum annihilations) is 11.4 (10.5) pions, 2.4 (2.2) kaons, 0.6 (0.5) ρ^0, 1.2 (0.8) K^*, 0.6 (0.4) protons and antiprotons, 0.15 (0.08) ϕ, 0.19 (0.07) Λ and $\bar{\Lambda}$, and 0.016 (0.005) Ξ^- and $\bar{\Xi}^+$. We have also seen evidence for η and f^0 production. The most significant differences between upsilon and continuum final states are (1) the inclusive energy spectra fall off more rapidly with increasing particle energy in upsilon decays, (2) the production of heavier particles, especially baryons, is not as strongly suppressed in upsilon decays, and (3) baryon and antibaryon are more likely to be correlated at long range in upsilon decay than in continuum events.

I. INTRODUCTION

The cross section for the annihilation of electrons and positrons into hadronic final states shows three narrow resonances in the center-of-mass energy range between 9.46 and 10.35 GeV, corresponding to the three ^3S bound states of the $b\bar{b}$ system, the $\Upsilon(1S)$, $\Upsilon(2S)$, and $\Upsilon(3S)$. The $\Upsilon(2S)$ and $\Upsilon(3S)$ states can decay to the $\Upsilon(1S)$, but the strong decays of the $\Upsilon(1S)$, which amount to about 80% of all $\Upsilon(1S)$ decays, must proceed through the annihilation of the b and $\bar{b}$ quarks to final states containing hadrons made of lighter quarks. In the lowest order of quantum chromodynamics (QCD), these strong decays go through an intermediate states of three gluons.[1] The observed decay products are then the result of the hadronization of the gluons. There is evidence that the directions of the final hadrons preserve some memory of the directions of the three gluons,[2] but at the energy of the upsilon the three hadron jets are typically rather broad and overlapping.

Electron-positron annihilation at energies away from the resonances proceeds through the single-photon intermediate state to the creation of a quark-antiquark pair which subsequently hadronizes into the observed final-state particles. In this case, the hadrons are emitted generally into two opposite jets centered on the directions of the quark-antiquark pair, provided that the quark masses are small compared with the total center-of-mass energy in the e^+e^- collision. At energies above 10.54 GeV the annihilation can produce $b\bar{b}$ pairs, which near threshold do not result in collimated jets but form pairs of B mesons and other excited states.

In this paper we study and compare the energy spectra and correlations of various hadron species from two data samples obtained with the CLEO detector at the Cornell Electron Storage Ring (CESR): (a) the strong decays of the $\Upsilon(1S)$, representing the hadronization of three gluons of total energy 9.46 GeV, and (b) the nonresonant annihilation of e^+e^- in the center-of-mass energy range between the $\Upsilon(3S)$ and the $B\bar{B}$ threshold, representing hadronization of quark-antiquark pairs ($u\bar{u}$, $d\bar{d}$, $s\bar{s}$, or $c\bar{c}$) with total energy 10.49 GeV. We will emphasize the attempt to understand the mechanisms for production of strangeness and baryon number in quark and gluon hadronization. Certain related topics, covered in other publications, will *not* be covered in detail in this paper: event-shape analyses (thrust, triplicity, etc.),[2] gluon bremsstrahlung,[3] charmed-meson production,[4] e^+e^- annihilation above the $B\bar{B}$ threshold,[5] and decays of higher upsilon states.[6]

II. DESCRIPTION OF THE CLEO DETECTOR

Figure 1 shows sections of the CLEO apparatus perpendicular and parallel to the colliding beams. Detailed descriptions of its various components have been published elsewhere.[7] We will therefore describe the detector only briefly in this paper.

A. Inner detector

A 3.2-m-long, 2-m-diameter superconducting solenoid produces a 10-kG longitudinal magnetic field uniform

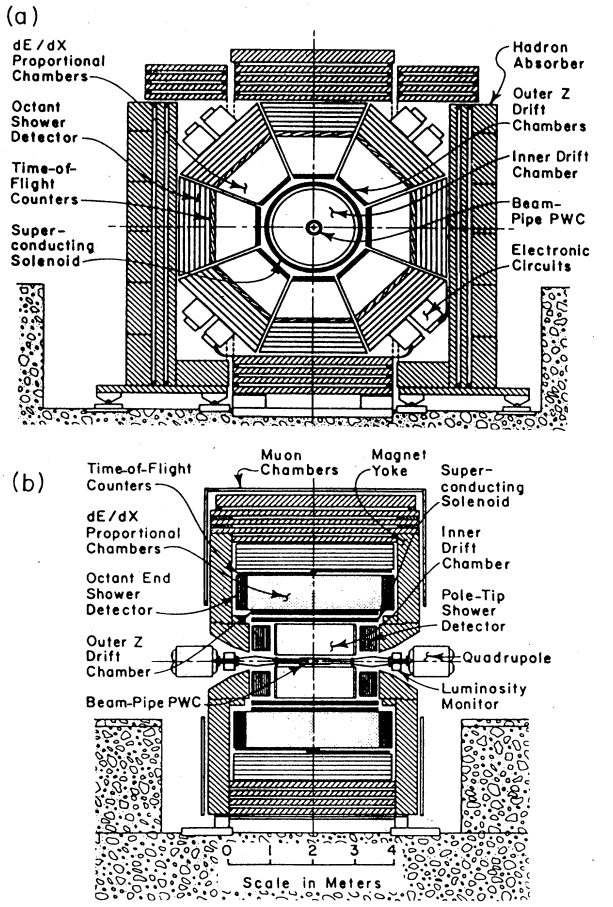

FIG. 1. End and side views of the CLEO detector.

over the volume of the tracking chambers (described below) to better than 0.5%. The radial thickness of the coil is 0.7 radiation lengths or 0.16 pion nuclear interaction lengths.

Inside the solenoid are proportional and drift chambers for tracking charged particles, and shower detectors mounted on each magnet pole to detect and measure the energy of photons and electrons produced at small angles to the beam.

The cylindrical drift chamber is the principal device for measuring momenta of charged particles. It has an inner radius 0.17 m, outer radius 0.95 m, and length 1.93 m. Sense wires form 17 concentric equally spaced cylinders of which 9 have axial wires and 8 have wires slanted at $\pm 2.915°$ to the longitudinal axis. The solid angle for particles which reach at least the seventh cylinder is $\Omega = 0.92 \times 4\pi$ steradians. The transverse-momentum resolution (rms) for particles which pass through 17 cylinders ($\Omega = 0.73 \times 4\pi$) is

$$(\delta p_T / p_T)^2 = [0.01p\ (\text{GeV})]^2 + 0.01^2 .$$

The first term is the curvature error due to position resolution in the drift chamber (about 200 μm), and the second term comes from multiple scattering in the chamber. The efficiency per cylinder is typically 90%,

the inefficiency coming from dead wires or electronic channels, bad calibrations, overlapping tracks, decays, and the tails of the spatial resolution function.

A proportional wire chamber surrounds the 2-mm-thick, 15-cm-diameter aluminum beam pipe. It consists of a triplet of nested cylindrical proportional wire chambers, with anode wires parallel to the beam line. The cathodes consist of 5-mm-wide strips in the form of hoops that encircle the beam axis. Information from the anode wires is used as a part of the fast trigger, in the event filter to reject events due to interactions of off-energy electrons with the walls of the beam pipe, and as an aid in track finding. Low-momentum charged hadrons can be identified by use of the pulse-height information from the anode wires.

The pole-tip shower detectors comprise one of three sets of shower counters in CLEO. The other two are identified as octant shower detector and octant end shower detector in Fig. 1. They are all made of rectangular proportional tubes interleaved with lead sheets. Table I gives the specifications of the various shower detectors.

Surrounding the beam pipe at a distance of 2.0 m on each side of the interaction point are four scintillator telescopes, which detect small-angle elastic (Bhabha) e^+e^- scatters. For any data run, the ratio of the number of coincidences to the QED Bhabha-scattering cross section defines the time-integrated beam luminosity.

B. Outer detector

Outside the magnet coil in order of increasing distance from the interaction region are the following outer-detector components.

(1) Three drift-chamber planes. These provide a measurement of the longitudinal coordinate for charged-particle tracks and help to identify hadrons and photons which have interacted in the coil.

(2) dE/dx chambers. These are multiwire proportional chambers filled with 91% argon, 9% methane and operating at 45 psi.[8] 117 samples of dE/dx are measured over a total path length of 79 cm. The rms resolution in the mean of the lowest 50% of pulse heights for tracks with at least 90 samples is 5.8%. This measurement together with the momentum measurement in the drift chamber provides particle identification over the momentum ranges shown in Table I.

(3) Time-of-flight scintillation counters. A total of 96 counters are located at about 2.3 m from the interaction region. Each scintillator is 25-mm thick, 2.032-m long, and 31.8-cm wide and is viewed by a single photomultiplier. They cover the polar angle range from 45° to 135° in two segments, and the full azimuthal range in 48 segments. The rms time resolution is 400 ps. Time-of-flight measurements provide an independent means of particle identification. The scintillation counters are also used in several of the trigger options.

(4) Electromagnetic shower counters. These are the principal shower counters of the detector. They cover a solid angle $\Omega = 0.47 \times 4\pi$ steradians and are essential for both electron and neutral-pion identification. They are used in the trigger, and provide the most reliable absolute measure of luminosity.

The four components discussed thus far are located outside the coil and are assembled in octants. Each octant is a structural unit which includes all its associated electronics.

TABLE I. CLEO detector specifications (resolutions are rms).

Charged particles: drift and proportional chambers			
$\Omega/4\pi$		0.92	
$(\delta p_T/p_T)^2$ with $B=10$ kG		$[0.012\ p\ (\text{GeV})]^2 + 0.01^2$	
$\delta\theta$ (radians)		$0.01 \sin^2\theta$ for $45° < \theta < 135°$	
$\delta\phi$ (radians)		0.002	
Photons and electrons: proportional tubes and lead			
	Octant	Octant end	Pole tip
θ (degrees)	>55	40—50	13—30
$\Omega/4\pi$	0.47	0.11	0.12
$\delta E/\sqrt{E}$ ($\text{GeV}^{1/2}$)	0.17	0.65	0.38
$\delta\theta$ (radians)	0.003	0.003	0.003
2γ separation (radians)	0.08	0.03	0.03
Hadron identification:	**Scintillators**		***dE/dx* proportional chambers**
$\Omega/4\pi$	0.56		0.56
Resolution	400 ps		5.8%
p (GeV) for π/K	<1.0		<0.8
p (GeV) for K/p	<1.45		<1.35
p (GeV) to traverse coil	$\pi > 0.2$,	$K > 0.45$,	$p > 0.65$
Muon identification: drift chambers			
$\Omega/4\pi$			0.78
E (GeV) to traverse iron			1—2

(5) Muon detector. The iron of the magnet is part of the hadron absorber for the muon detector. Drift chambers are located at various depths in the iron to detect penetrating charged particles. Some chambers are mounted directly on the magnet yoke and others are on four movable carts carrying additional iron.

III. SELECTION OF HADRONIC ANNIHILATION EVENTS

A. The hardware trigger

The beams intersected in the center of the detector 400 000 times per second. An appreciable fraction of these beam crossings were accompanied by a signal in several of the 20 000 data channels, representing ionization collected by various drift-chamber or proportional-chamber wires, or scintillation counters. It would have been prohibitively time consuming to read out, record, and analyze all of these signals. We relied on a sophisticated trigger system to decide whether there might be an interesting event to be saved.

Five components of the CLEO detector provided signals to the trigger system: the inner cylindrical proportional chamber surrounding the beam pipe, the large cylindrical drift chamber, the time-of-flight scintillation counters, the electromagnetic shower detectors arranged in octants, and the shower detectors mounted on the magnet poles. Charged-particle triggers were obtained from the fast track-segment processor, which in 1.5 μs found track candidates in the inner proportional chamber and the cylindrical drift chamber.[9] Typically, either one of the following two conditions constituted a valid trigger for hadronic events: (1) three processor tracks and hits in at least two octants of time-of-flight scintillators within 110 nsec of the beam crossing time, or (2) any two processor tracks, and hits in two opposite time-of-flight half-octants.

Condition (1) was the principal trigger for hadronic events. Condition (2) was designed to detect muon pairs; about 85% of the hadronic events pass it as well. Several other trigger conditions were also enabled. These were optimized for QED processes and for events with a large neutral energy fraction, and are of no relevance for our present measurements. With these conditions the total trigger rate was generally between 1 and 2 Hz.

The CLEO trigger as described above was sensitive to events with a charged multiplicity of at least three, provided at least two charged particles were within the 56% solid angle covered by the time-of-flight scintillators and had sufficient range to penetrate the solenoid coil. Events with just two charged tracks could trigger only if the two tracks were nearly collinear and hit the time-of-flight counters, or at least one particle (charged or neutral) deposited more than 1 GeV in the octant shower detector system, covering 47% solid angle. An event with no triggerable charged particles could be recorded only if more than 1 GeV of energy was deposited in each of two octants or ends of the shower detection systems. It was unfortunately not possible to run the CLEO detector using an unrestricted two-charged-particle trigger, without an unacceptable background rate.

B. Analysis cuts

The data recorded by the hardware trigger included not only the desired hadronic annihilation events, comprising about 3% of the total sample [up to 20% when running on the $\Upsilon(1S)$], but also background from beam-gas and beam-wall collisions, cosmic rays, QED processes (e^+e^-, $\mu^+\mu^-$, $\tau^+\tau^-$, $e^+e^-\gamma$, etc.), and the two-photon-collision process ($e^+e^-\rightarrow e^+e^-X$). We imposed requirements on the reconstructed events in order to reduce or eliminate these backgrounds.

The CLEO data-reduction program reconstructed charged-particle tracks from the cylindrical-drift-chamber data, determining the momentum components for each charged track in its sensitive volume, corresponding to $30° < \theta < 150°$ and $p > 100$ MeV/c. Using data from the detector components outside the solenoid coil, it also reconstructed photon showers over about 60% of the full solid angle, and identified e, μ, π, K, and p within favorable momentum and angle ranges.

To be accepted as a hadronic annihilation event for the purposes of the work described in this paper, an event had to satisfy the following requirements.

(1) Track quality. Charged-particle track candidates reconstructed in the large cylindrical drift chamber can be categorized as bad, poor, good, or excellent. A bad track candidate was one for which only the transverse (r,ϕ) projection could be reconstructed; there was no matching longitudinal (r,z) projection obtained from the slanted stereo wires. Such candidates were usually spurious reconstructions from uncorrelated wire hits, and were not included in the eventual data sample. A poor track was one which failed at least two of the following four criteria: an extrapolated z_0 at the beam line within 50 mm of the origin (nominal beam intersection), an extrapolated radius r_0 of closest approach to the beam line less than 5 mm, a rms residual less than 0.7 mm in the fit to a helix, and fewer than 10 missing hits along the track. All other tracks were called good, except those with $r_0 < 1.5$ mm, which were labeled excellent. To be accepted an event had to have at least one excellent track, and the ratio (bad + poor)/(excellent + good + poor) had to be less than 1.15. In addition, we required that at least 15% of the drift-chamber wire hits be associated with reconstructed tracks (not including bad tracks). The track quality requirements strongly suppressed background from beam-wall collisions which produce showers in the beam pipe resulting in many unreconstructable hits in the drift chamber. Essentially all hadronic events passed.

(2) Vertex. After the track pairs which reconstruct as K_S^0 or Λ decays or as photon conversions had been excluded, the remaining charged tracks were fit to a common event vertex. To be accepted this vertex had to be within 2 cm of the beam line in x and in y and within 5 cm longitudinally of the nominal beam intersection. This criterion rejected most beam-gas, beam-wall, and cosmic-ray events, and had practically no effect on the efficiency for hadronic events.

(3) Visible charged multiplicity. An accepted event had to have at least three detected charged tracks (excellent, good, or poor). The track count included the secondaries from K_S^0 and Λ decays but excluded recognized photon

conversions. We also rejected events having three or more charged prongs in which two of the particles had high energy and were oppositely directed while the remainder had very low energies. This was done by requiring that the ratio R_2 of Fox-Wolfram moments[10] H_2/H_0 be less than 0.98. R_2 is a convenient measure of the "two-jet" character of the event; it becomes 1.0 in the limit of an ideal two-body final state. The multiplicity requirement eliminated most e^+e^- and $\mu^+\mu^-$ events and most cosmic rays and considerably reduced the rate from $\tau^+\tau^-$ and the two-photon process. The R_2 requirement suppressed radiative Bhabha events ($e^+e^-\gamma$) in which the photon had converted. These cuts have a significant effect on the acceptance for hadronic events, which we must correct for (see Sec. III D below).

(4) Visible energy. This included the sum of the energies of all charged tracks reconstructed in the drift chamber (assuming pion masses), plus the energies of all detected electromagnetic showers unmatched to charged tracks. For hadronic annihilation events the visible energy should be close to the center-of-mass beam energy W, except for the effects of measurement error, gaps in the geometrical aperture, missing K_L^0, n, and ν. Actually, we observe a broad distribution centered somewhat below W. To be accepted, a hadronic event had to have a visible energy at least 30% of W. We also required that the energy recorded in the octant shower counters be between 0.25 and 10.5 GeV. These requirements suppressed background from beam-gas, beam-wall, cosmic rays, $\tau^+\tau^-$, and the two-photon process. We must correct, however, for the 2% portion of the desired hadronic annihilation events which failed to show enough visible energy because of the loss of particles from the accepted solid angle.

(5) Visible-momentum balance. Except for the effects of undetected particles and momentum measurement error, hadronic annihilation events should balance momentum. Since beam-gas, beam-wall, and cosmic-ray events involve an initial net momentum, their products in the detector will not balance in general, nor will two-photon-collision events in which the outgoing electron and/or positron is emitted at too small an angle to be detected. A convenient measure of the momentum imbalance is the ratio R_1 of Fox-Wolfram moments[10] H_1/H_0; $R_1=0$ for a perfectly balanced event. We required that an accepted event have $R_1<0.4$. About 2% of hadronic events failed this requirement, usually because of undetected particles.

(6) Radiative Bhabha exclusion. After the application of the above requirements the data sample still contained a contamination from radiative Bhabha scattering ($e^+e^-\gamma$) followed by photon conversion or showering in the beam pipe. To eliminate this remaining background we rejected all events of observed multiplicity ≤ 6 which contained two oppositely directed high momentum showering charged tracks. Although this had little or no effect on the acceptance for hadronic annihilation events from the $\Upsilon(1S)$ or the continuum, which are our concern in this paper, such a requirement would have been inappropriate for $\Upsilon(2S)$ and $\Upsilon(3S)$ running, since it rejected events in which the higher upsilon state decayed via $\pi\pi$ or γ emission to the $\Upsilon(1S)$ followed by $\Upsilon(1S)\rightarrow e^+e^-$.

Not all of the above requirements were applied to the data after the events were completely reconstructed. In order to reduce the computation time spent in trackfinding for bad events, we applied each cut as early as possible in the analysis chain.

C. Backgrounds

The continuum event sample surviving the analysis cuts listed above contains less than 0.6% of events which are not beam-beam collisions: that is, beam-gas, beam-wall, and cosmic-ray events. This is seen from the distribution of the longitudinal (z) coordinate of the reconstructed vertices (Fig. 2) for events which passed all of the requirements except the z vertex cut, which was ignored in this plot. The flat rate at large $|z_v|$, extrapolated under the main peak within the cuts, gives the quoted background level.

From a visual scan of a subset of the accepted continuum event sample we estimate that the contamination of radiative Bhabha events is less than 3%. The remaining background comes from the $\tau^+\tau^-$ and two-photon processes. Both contribute mainly to the low multiplicity channels and are often indistinguishable from low multiplicity hadronic annihilation events. We have simulated both processes with Monte Carlo programs. In the case of $e^+e^-\rightarrow\tau^+\tau^-$ the production cross section ($R=1$) and decay branching ratios[11] are well known. The cross section and event topologies for $e^+e^-\rightarrow e^+e^-X$ can probably be estimated within 20%. In both cases we propagated generated events through a simulation of the CLEO detector, taking account of the bending of charged particles in the solenoid field, ionization energy loss and Coulomb scattering by charged particles, radiation by electrons, Compton scattering and pair production by photons, nuclear absorption, and decays. Secondary particles from radiation, pair production, and decay were also tracked. The calculation was carried through in detail for the tracking chambers inside the solenoid, including the simulation of raw data with the known sense wire efficiencies and resolutions. In the outer detector simplified algorithms were used, taking account only of the geometry and the generalized performance of the detector

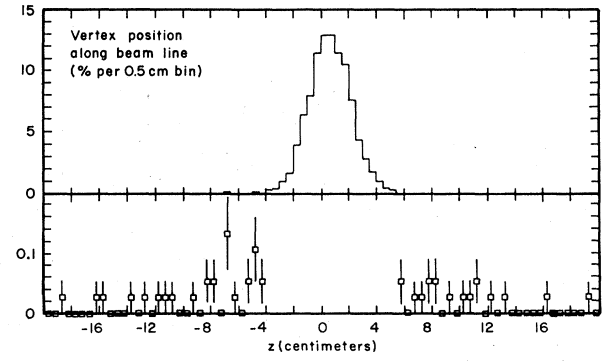

FIG. 2. Typical distribution of reconstructed vertices of e^+e^- hadronic annihilation events along the beam axis. The acceptance requirement in this variable ($|z|<5$ cm) is relaxed in order to display the distribution.

modules, since a detailed following of the history of each particle would have been rather time consuming and unnecessary for the acceptance calculation. The simulated data were analyzed just as if they were real data events, in order to determine what fraction pass the various criteria listed above for hadronic annihilation events. The results for the contribution to the apparent R value from the two processes are $\Delta R=0.17\pm0.02$ for $\tau^+\tau^-$ and $\Delta R=0.12\pm0.05$ for the two-photon collisions. Including all backgrounds, the net estimated contamination in our continuum hadronic annihilation data sample is 7%.

All of the backgrounds we have mentioned are practically independent of beam energy over the range $W=9$ to 11 GeV. When we derive a rate for the $\Upsilon(1S)$ decays by subtracting the measured continuum rate from the rate measured at the peak of the resonance, we automatically subtract all backgrounds as well. The resonance event rates can therefore be considered background free.

D. Acceptance

The Monte Carlo program, which simulated the nonresonant production of hadrons, generated jetlike events using the Lund version[12] of the Feynman and Field model[13] for quark fragmentation. The primary pair was produced with a probability proportional to the square of the quark charge, and defined an axis in space, the jet axis, which was preserved throughout the hadronization chain. Subsequent quark-antiquark pairs were generated with a Gaussian distribution of transverse momentum having a root-mean-square value of 350 MeV/c. Each generated antiquark combined with the quark from the preceding generation to form a meson. Baryon production was included by generating diquark pairs. The spin of each meson was chosen randomly, either zero or one with equal probability. The transverse momentum of the meson was the vector sum of the quark and antiquark transverse momenta. Finally, the longitudinal momentum p_L of the meson was determined using the Field-Feynman fragmentation function[13] $f(x_F)$. The variable x_F is the $E+p_L$ of the meson, divided by that for the whole jet, and $f(x_F)$ gives the probability density (per unit x_F) for the created meson. Energy and momentum were conserved at each step of the chain. The model allows gluon bremsstrahlung, the fragmentation of the gluon proceeding similarly to quark fragmentation.

The simulation of the three-gluon-mediated decay of the upsilon proceeded as follows. Each of the three gluons decayed into a quark-antiquark pair, then a quark from each gluon together with an antiquark from one of the other gluons hadronized in the $q\bar{q}$ center-of-mass frame in the same manner as a continuum produced $q\bar{q}$ pair of the same center-of-mass energy.

The Monte Carlo program tracked each produced particle through a simulation of the CLEO detector, taking account of the same physical processes discussed above in connection with the simulation of the backgrounds. We produced artificial raw data, which we then reconstructed with the same programs used on the real data, determining the acceptance from the proportion of events satisfying the analysis cuts. Since the analysis requirements were more stringent than any of the hardware trigger conditions, we ignored any additional effect of trigger acceptance. In a previous publication[9] we have discussed in detail the tests of the validity of our Monte Carlo simulation and the systematic uncertainties. We estimate a systematic error of 2%, by noting the effect of making variations in the Monte Carlo input assumptions which did not significantly alter the agreement of the distributions compared with data. The overall acceptance for continuum $q\bar{q}$ events is 79.6%; for the upsilon decays into ggg it is 89.4%. Figure 3 shows the acceptance as a function of the observed number of charged tracks.

E. Data samples

The continuum data correspond to a total accumulated luminosity of 17.3 pb^{-1} of running at energies between the $\Upsilon(3S)$ resonance and the $B\bar{B}$ threshold (see Table II for details), a range of 0.18 GeV centered on $W=10.49$ GeV. The number of observed events satisfying our criteria, 55 328, becomes 51 188 after background subtraction and yields a net 64 306 after acceptance correction (Table II).

For most of the results reported here the $\Upsilon(1S)$ data sample consists of 2.65 pb^{-1} of running at the peak of the resonance, $W=9.46$ GeV. The number of observed events passing our analysis cuts was 61 193. This is reduced to 50 742 after subtracting the continuum contribution, obtained by rescaling the raw number of events observed in the continuum running to account for the integrated luminosity and the W^{-2} dependence of the continuum cross section (see Table II). This subtraction also corrects for any nonresonant backgrounds, since they should contribute equally to the upsilon and continuum rates. The upsilon number is further reduced by 10.4% to give 45 465, the estimated number of "direct" hadronic decays. The 10.4% is the fraction of observed upsilons decaying electromagnetically through quark-antiquark pairs, calculated from the leptonic branching ratio $B_{\mu\mu}=0.028\pm0.003$,[14] the measured R value (3.8 ± 0.3) in the nearby continuum,[9]

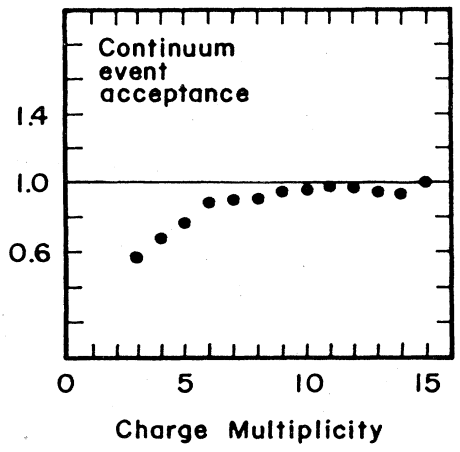

FIG. 3. The acceptance of continuum hadronic annihilation events as a function of the number of charged tracks seen in the detector.

TABLE II. Data samples.

	Continuum	$\Upsilon(1S)$
Minimum center-of-mass energy W (GeV)	10.376	9.456
Maximum W (GeV)	10.558	9.463
Mean energy $\overline{W}$ (GeV)	10.49	9.460
Integrated luminosity L (nb^{-1})	17252	2651
Background scaling factor $r=L_{\rm on}\overline{W}^2/(L_{\rm off}M_\Upsilon{}^2)$		0.1889
Events passing acceptance requirements	55328	61193
Background to be subtracted	$4140=0.24L$	$10451=rN_{\rm off}$
Events after subtraction	51188	$50742=N_\Upsilon$
$f_\gamma=(\Upsilon\to q\bar{q})/(\Upsilon\to\text{total})$		0.104
Events from Υ "direct"$=(1-f_\gamma)N_\Upsilon$		45465
ϵ=event acceptance	0.796	0.894
Corrected number of events	64306	50856

and the relative acceptance $a=\epsilon_{qq}/\epsilon_{ggg}=0.89\pm0.03$ for the continuum and direct-decay events:

$$f_\gamma=RB_{\mu\mu}/(1-3B_{\mu\mu})=0.115\pm0.011\ ,$$

$$f_{\gamma\rm obs}=af_\gamma/[1-(1-a)f_\gamma]=0.104\pm0.013\ .$$

Finally, after correcting for acceptance, we estimate the number of upsilon direct decays corresponding to our integrated luminosity to be 50856.

Since most of our results in this paper on yields of various particle species will be quoted and compared in terms of particles per event, these corrected numbers of continuum and upsilon-direct events will be used as normalization.

IV. STABLE OR LONG-LIVED CHARGED HADRONS: π, K, AND p

A. Hadron identification

To identify charged hadrons we used the dE/dx proportional chambers and the time-of-flight scintillation counters. The time-of-flight system is capable of separating kaons and pions over a momentum range from 0.55 to 1.00 GeV/c and identifying protons from 0.85 to 1.45 GeV/c (see Fig. 4). The dE/dx system is effective for pions and kaons from 0.45 to 0.80 GeV/c and for protons from 0.65 to 1.35 GeV/c (see Fig. 5). The lower limits are set by energy loss and absorption, mainly in the solenoid coil. The upper limits are determined by the resolution of each device.

A particle was identified in the scintillators as being a kaon or a proton by requiring that the candidate have a measured time of flight within 0.8 ns of the time expected for that hypothesis (this corresponds to two standard deviations in the time measurement) and outside of 0.8 ns of the time expected for any other hypothesis. Any particle within 0.8 ns of the expected pion time was assumed to be a pion.

In the octant proportional-wire-chamber modules a track was considered to be a kaon if its measured ionization was between -2 and $+3$ standard deviations of that expected for a kaon and outside 2 standard deviations of that expected for a pion. One standard deviation was typ-

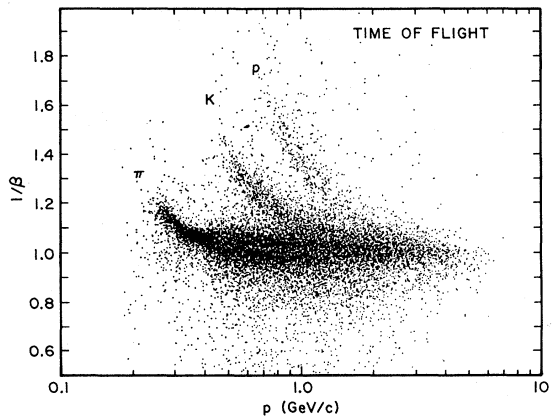

FIG. 4. Typical scatter plot of $1/\beta$, derived from measured flight times, versus track momentum measured in the cylindrical drift chamber. Interactions in the solenoid coil between the drift chamber and the time-of-flight scintillator system are the chief cause of the measurements which fall outside the expected bands for π, K, and p.

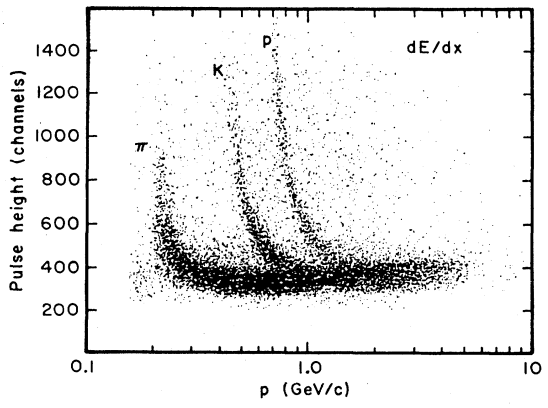

FIG. 5. Typical scatter plot of dE/dx measured in the octant proportional chambers versus momentum measured in the cylindrical drift chamber. Interactions in the solenoid coil between the drift chamber and the dE/dx chamber system are the chief cause of the measurements which fall outside the expected bands for π, K, and p.

ically 6% of the measured ionization. Particles were assumed to be pions (with a muon background) if they came within 2 standard deviations of the expected pion ionization. Particles were identified as protons if the measured ionization was within -2 and $+3$ standard deviations of that expected for protons and outside 2 standard deviations of that expected for kaons or pions.

Of the tracks which were accepted as identified, about one third were identified by both time of flight and ionization. For the remaining two thirds, one of the two systems provided no useful information, because of inefficiencies caused by track confusion, overlaps, interactions, edge effects, and fluctuations.

Above about 2.5 GeV/c the dE/dx system can be used only to identify pions on a statistical basis. In this region, we could determine the number of pions by fitting a plot of the measured dE/dx pulse heights. Figure 6 shows one such plot, fitted with two Gaussians. Because of our resolution, we cannot separate kaons and protons; we can fit them with a single Gaussian. The widths and relative separation of the two peaks were consistent with our expectations. The tail to the right of the pion peak is due to electrons.

Low-momentum charged particles cannot reach the time-of-flight scintillators or dE/dx chambers located outside the coil. For these particles we used ionization information from the inner cylindrical proportional chamber surrounding the beam pipe. This chamber provided us with three samples of dE/dx along a charged track. We accepted a track if there was at least one hit wire along the track in each of the three layers, and if there was no overlap with another charged track within two adjacent wires. We took a weighted sum of the three pulse heights by adding $\frac{2}{3}$ of the lowest to $\frac{1}{3}$ of the middle pulse height, and discarding the highest one. This gave the same result as a maximum-likelihood calculation. Figure 7(a) shows the distribution of squared masses calculated from the weighted pulse height average and the momentum measured in the large drift chamber, for upsilon data in the x range from 0.07 to 0.08. The Landau tail of the pion dE/dx distribution dominates even in the mass region where one expects peaks from the kaons and protons, so we devised a procedure for subtracting statistically the pion contribution. Figure 7(b) shows the distribution for particles (pions, mainly) which had sufficient range to reach the outer chambers. The rates for kaons and protons were obtained by subtracting from the original mass-squared spectrum [Fig. 7(a)] the spectrum for pions [Fig. 7(b)] normalized to the same area below $m^2=0.08$ GeV^2. The difference spectrum [Fig. 7(c)] shows the contributions of the kaons and protons. Because of the high background of low-momentum protons from beam-gas collisions, our quoted proton-and-antiproton rates determined from the inner proportional chamber are actually the observed antiproton rates, doubled.

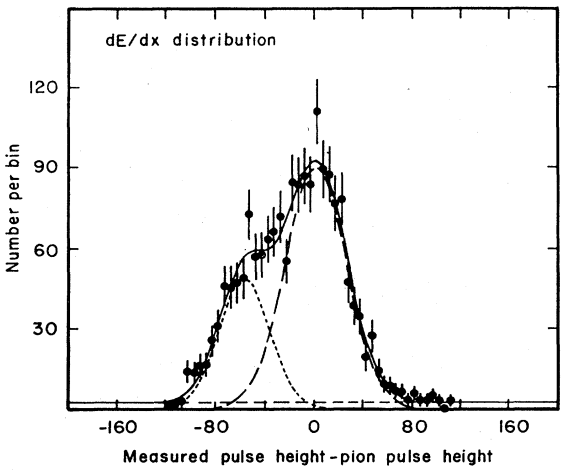

FIG. 6. Spectrum of measured dE/dx for charged tracks in the momentum range 3.0 to 3.5 GeV/c, plotted in terms of the average pulse-height channel number minus the number predicted for pions. The data are fitted to two Gaussians plus a flat background. The peak centered at 0 is interpreted as pions, the smaller peak is due to kaons and protons, which have indistinguishable dE/dx at these momenta. The tail on the right is due to electrons.

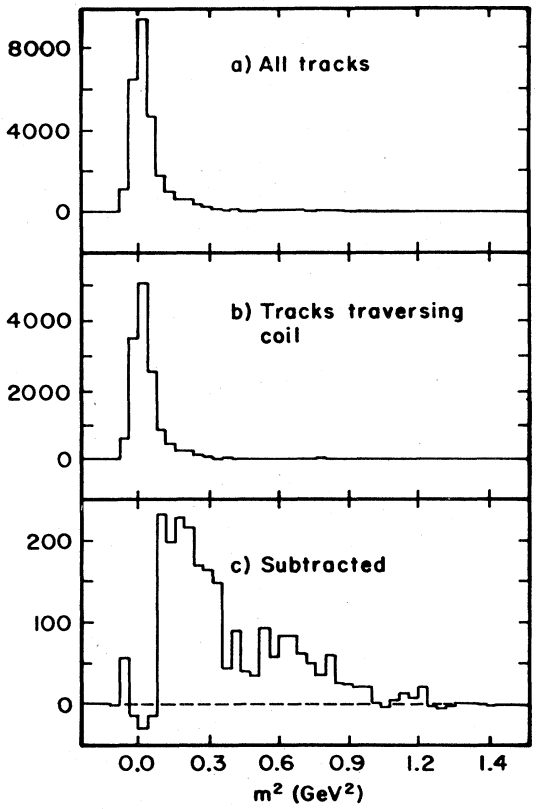

FIG. 7. Sample distributions of measured particle mass squared, derived from the ionization energy loss in the three layers of the beam-pipe proportional chamber and the momentum measured in the large cylindrical drift chamber: (a) for all charged particles in the momentum range 330 to 380 MeV/c; (b) for those particles which have sufficient range to penetrate the solenoid coil and reach the outer planar drift chambers; (c) the difference between (a) and (b) normalized to match below $m^2=0.08$ GeV^2.

B. Calculation of the inclusive rate

For each particle type, and for on and off resonance data samples, we accumulated the numbers of tracks n in two-dimensional bins of fixed $x=2p/W$ and fixed observed charged multiplicity ν. For each bin we obtained the contribution from the upsilon resonance by subtracting the raw continuum background (Δn refers to tracks in one bin of x):

$$\Delta n_{\Upsilon}=\Delta n_{\rm on}-r\,\Delta n_{\rm off}\ ,$$

where

$$r=L_{\rm on}\overline{W}_{\rm off}{}^2/(L_{\rm off}M_{\Upsilon}{}^2)\ ,$$

the ratio of accumulated luminosities, scaled by the energy dependence of the continuum cross section. For our data samples r was 0.189 (see Table II). We then corrected the continuum yields bin by bin for the contamination from $\tau^+\tau^-$ and two-photon events (up to 20% in the lowest-multiplicity bins), evaluated by Monte Carlo simulation.

At this point we subtracted the backgrounds in the upsilon and continuum samples. For pions, these backgrounds included muons (2 to 3% of the identified pion sample) and an insignificant contamination of electrons, kaons, and protons. For the identified kaons, the background was mainly misidentified pions (10 to 30%). It was determined from the number of particles for which the dE/dx and time of flight systems gave conflicting identifications. For identified protons, the backgrounds included misidentified pions and kaons (8 to 30%) and protons from secondary interactions in the beam pipe or the coil. Again, the former was measured by the number of times the dE/dx and scintillator identifications disagreed. The latter was essentially eliminated by strict cuts on the extrapolated track origin and by cuts on the angular deflection of the particle in passing through the coil.

The subtraction for the inclusive spectrum of upsilon "direct" is subtle, because the x spectrum from $\Upsilon\to q\bar{q}$ events scales in shape with the $q\bar{q}$ continuum spectrum, while the overall magnitude depends also on the product of $f_{\gamma\rm obs}$ (the acceptance corrected fraction of Υ hadronic decays going via $\Upsilon\to\gamma_{\rm virt}\to q\bar{q}$) and the total Υ rate. The correct expression for the upsilon direct rate for a given x,ν bin is

$$\Delta n_{\rm dir}=\Delta n_{\Upsilon}-f_{\gamma\rm obs}(N_{\rm on}/N_{\rm off}-r)\Delta n_{\rm off}\ .$$

For our data the coefficient of the continuum rate $\Delta n_{\rm off}$ was 0.0954 (see Table II). Note that in this paper n always refers to a number of particles of some given species, while N refers to a number of events.

In order to minimize the model dependence of our Monte Carlo acceptance calculations we used the following procedure to correct the inclusive distributions. The calculations of the acceptance for two-jet and three-jet events, described above in Sec. III D, were tabulated also as functions of ν, the visible number of charged tracks (excluding photon conversions). Figure 3 shows this acceptance for continuum data. We used these ν-dependent event acceptances to correct the observed yields for each multiplicity bin, then summed over ν bins starting at the minimum $\nu=3$. For each particle, from upsilon direct and continuum, and for each x bin this sum was then corrected for the fraction of events which fell below $\nu=3$ in the corresponding Monte Carlo calculation. Finally, we corrected each yield for the probability that the given particle of specified x in an accepted event would itself be detected. This factor was obtained for each x and ν bin. It ranged from 40 to 50% for low multiplicity events and approached 70% for high multiplicity. It included drift chamber tracking acceptance (94%) and a geometric acceptance factor which depended on the shape characteristics of the event. The acceptance for particle identification was determined directly from the data for pions, using a Monte Carlo simulation to correct for effects such as differing decay rates and interaction probabilities. This acceptance was about 35%, and gave an overall probability of 25 to 30% for finding and identifying a charged hadron in an accepted event. Note that our method of correcting for acceptance took account of any correlations between the probability of observing a track of fractional momentum x and the multiplicity of the event, with minimum dependence on the model assumptions in the Monte Carlo event generator. The net efficiencies for pions, kaons, and protons including event acceptance, geometrical aperture, and identification probability are summarized for continuum events in Table III.

In the momentum range 0.45 to 1.45 GeV/c in which charged hadrons are identified by time-of-flight and dE/dx measurements, we may divide the systematic uncertainties into two categories, those associated with the Monte Carlo simulation of the events and of the detector, and those resulting from the analysis procedure itself. In the former category we include such things as hadronic event acceptance and backgrounds (10%), particle interactions in the material between the interaction point and the outer detector (8%), the uncertainty in the momentum of a particle due to its energy loss in the solenoid coil (4%), and the effect of decays in flight (typically 5%). The latter category includes such things as the performance of the time-of-flight and dE/dx detector elements and the subtraction of the background due to misidentification, and amounted to 10 to 20%, depending on the particle type and momentum. The overall systematic uncertainty for kaons and protons averaged 16% in the momentum range for which we could identify them. It had a minimum value 14% in the middle of the range and increased to about 20% near the lower and upper ends. For pions the systematic uncertainty was estimated to be 12 to 15%. From point to point in the momentum spectra the systematic errors are highly correlated. It is not too far from the truth to think of them as a common scale uncertainty affecting all the data in a given spectrum.

In the low-momentum range, in which we measured the pion, kaon, and proton rates by ionization in the beam-pipe proportional chamber, the systematic uncertainty was 10 to 12% for kaons and protons, and smaller for pions. The major contributing causes were sensitivity to the 0.08-GeV^2 mass-squared cut in the subtraction normalization and range straggling in the solenoid coil.

TABLE III. Particle detection and identification efficiency.

Hadron	p (GeV/c)	Typical efficiency	Method
π^+,π^-	0.15–0.55	0.36	dE/dx in inner proportional chamber (PC)
	0.45–0.80	0.07	dE/dx in outer PC
	0.55–1.00	0.10	time of flight
	>2.5	0.3	dE/dx in order PC (statistical)
K^+,K^-	0.25–0.35	0.26	dE/dx in inner PC
	0.45–0.80	0.04	dE/dx in outer PC
	0.55–1.00	0.08	time of flight
$p,\bar{p}$	0.40–0.55	0.31	dE/dx in inner PC
	0.65–1.35	0.07	dE/dx in outer PC
	0.85–1.45	0.07	time of flight
π^0	>0.5	0.06	$\pi^0\to\gamma\gamma$ in shower detector
$K^0,\bar{K}^0$	>0.25	0.07	$K_S^0\to\pi^+\pi^-$
$\Lambda,\bar{\Lambda}$	>0.5	0.06	$\Lambda\to p\pi^-$
$\Xi^-,\bar{\Xi}^+$	>0.75	0.08	$\Xi^-\to\Lambda\pi^-$
ρ^0	>0.75	0.5	$\rho^0\to\pi^+\pi^-$
K^{*+},K^{*-}	>0	0.010	$K^{*+}\to K_S^0\pi^+$
$K^{*0},\bar{K}^{*0}$	>0	0.014	$K^{*0}\to K^+\pi^-$
ϕ	>1.0	0.36	$\phi\to K^+K^-$

C. Inclusive-spectrum results

For convenience in the calculation of the single particle inclusive spectra we have chosen bins of fixed fractional particle momentum, $x=2p/W$. Figures 8 and 9 and Table IV show the charged pion, kaon, and proton spectra for continuum and upsilon-direct decays plotted as the average number n of the specified particles per unit interval of x, divided by the number N of hadronic annihilation events, that is, $(1/N)dn/dx$ or equivalently $(1/\sigma_{\text{total}})d\sigma/dx$. Within errors the positive and negative particle yields are equal; they are summed in the plots.

Figure 10 shows the same data plotted as particle fractions. At low momenta pions dominate. As x approaches one, the kaon and proton fractions increase to about 30% and 5%, respectively, in the continuum, and 40% and 10% in upsilon decays. The low-momentum pion excess

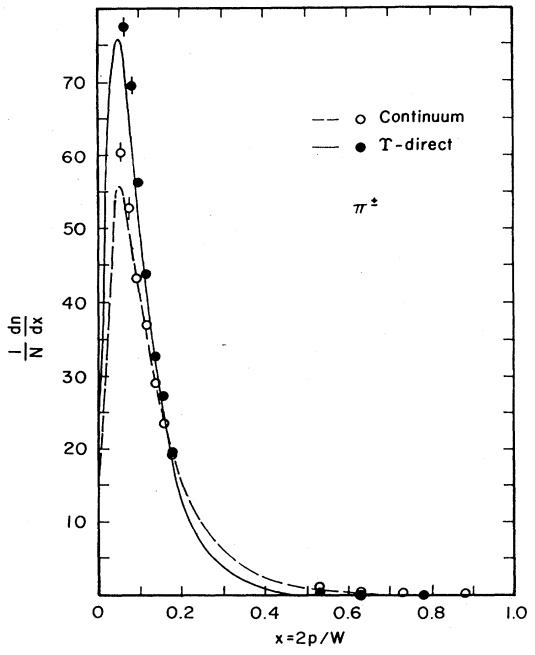

FIG. 8. Charged-pion (π^+ and π^-, summed) inclusive spectra, plotted as the mean number per event per unit x, versus x, where x is the particle momentum divided by the beam energy $W/2$. Spectra are plotted for nonresonant continuum events (open circles) and for upsilon strong decays (closed circles). The indicated errors are statistical only; systematic errors are given in Table IV. The curves show the fits described in the text.

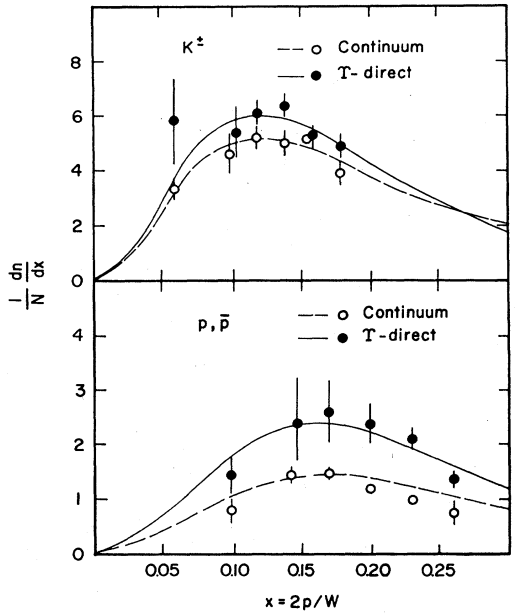

FIG. 9. Charged-kaon and proton-antiproton spectra in x. The indicated errors are statistical only; systematic errors are given in Table IV. The curves show the fits described in the text.

TABLE IV. Inclusive spectra (mean particles per event per unit $x = 2p/W$). Errors are statistical, followed by systematic.

Hadron	$\langle x \rangle$	Continuum $(1/N)dn/dx$	Upsilon $(1/N)dn/dx$
π^+,π^-	0.06	60.7±1.5±2.1	77.3±1.7±3.3
	0.08	52.8±1.3±2.4	69.7±1.5±3.1
	0.10	43.6±0.5±5.6	56.7±1.3±2.6
	0.105		52.9±0.04±7.4
	0.12	36.9±0.02±4.4	43.8±0.04±5.7
	0.14	29.0±0.02±3.5	32.6±0.04±3.9
	0.16	23.5±0.02±2.8	27.2±0.04±3.3
	0.18	19.5±0.01±2.5	19.7±0.04±2.6
	0.53	1.12±0.08±0.16	0.29±0.05±0.04
	0.63	0.52±0.05±0.07	0.09±0.02±0.02
	0.73	0.33±0.03±0.05	
	0.78		0.017±0.008±0.005
	0.88	0.17±0.02±0.02	
K^+,K^-	0.06	3.6±0.4±0.3	5.8±1.5±0.5
	0.10	4.7±0.7±0.9	
	0.105		5.4±0.9±1.1
	0.12	5.2±0.4±0.8	6.1±0.4±1.0
	0.14	5.0±0.4±0.7	6.4±0.4±0.9
	0.16	5.2±0.4±0.7	5.3±0.3±0.7
	0.18	3.9±0.4±1.0	4.9±0.4±1.2
$p,\bar{p}$	0.10	0.77±0.25±0.08[a]	1.45±0.30±0.15[a]
	0.1475	1.43±0.11±0.29	2.40±0.85±0.48
	0.17	1.47±0.10±0.22	2.60±0.54±0.39
	0.20	1.19±0.07±0.18	2.38±0.34±0.36
	0.23	0.98±0.09±0.14	2.10±0.19±0.29
	0.26	0.75±0.21±0.20	1.36±0.14±0.37
π^0	0.15	9.4±1.2±1.7	16.5±4.3±5.3
	0.25	3.8±0.5±0.4	3.8±0.5±0.7
	0.35	1.5±0.3±0.2	1.3±0.2±0.3
	0.45	0.91±0.28±0.16	0.26±0.07±0.05
$K^0,\bar{K}^0$	0.075	3.02±0.18±0.36	3.78±0.23±0.45
	0.125	3.65±0.16±0.44	5.38±0.22±0.66
	0.175	2.91±0.13±0.35	3.63±0.17±0.44
	0.225	2.31±0.11±0.28	3.04±0.14±0.36
	0.275	1.74±0.13±0.21	1.99±0.11±0.24
	0.325	1.30±0.08±0.16	1.12±0.09±0.13
	0.375	0.93±0.06±0.11	0.67±0.07±0.08
	0.425	0.60±0.05±0.07	0.37±0.05±0.04
	0.475	0.50±0.05±0.06	0.27±0.05±0.03
	0.525	0.26±0.03±0.03	0.12±0.03±0.02
	0.575	0.18±0.03±0.02	0.07±0.02±0.01
	0.625	0.088±0.019±0.010	0.064±0.020±0.008
	0.675	0.090±0.018±0.011	0.040±0.017±0.005
	0.725	0.034±0.012±0.004	0.028±0.013±0.003
	0.775	0.032±0.011±0.004	0.011±0.009±0.001
	0.825		0.017±0.008±0.002
	0.85	0.006±0.004±0.001	
	0.875		0.0006±0.0020±0.0001
$\Lambda,\bar{\Lambda}$	0.075	0.13±0.19±0.02	0.03±0.21±0.01
	0.125	0.26±0.07±0.03	0.84±0.11±0.10
	0.175	0.24±0.04±0.03	0.75±0.07±0.09
	0.225	0.21±0.03±0.03	0.61±0.05±0.07
	0.275	0.18±0.03±0.02	0.50±0.04±0.06
	0.325	0.13±0.02±0.02	0.34±0.04±0.04
	0.375	0.08±0.02±0.01	0.25±0.03±0.03
	0.45	0.067±0.012±0.008	0.137±0.017±0.016
	0.575	0.024±0.007±0.003	0.027±0.007±0.003
	0.725	0.005±0.004±0.001	0.001±0.003±0.001
	0.875	0.0±0.003±0.001	0.001±0.003±0.001
$\Xi^-,\bar{\Xi}^+$	0.25	0.013±0.005±0.002	0.066±0.015±0.007
	0.35	0.009±0.003±0.001	0.014±0.011±0.002
	0.45	0.003±0.002±0.001	0.009±0.007±0.001
	0.55	0.004±0.001±0.001	0.010±0.005±0.001
	0.65	0.0013±0.0015±0.0002	0.0040±0.0032±0.0005
ρ^0	0.15		1.90±0.43±0.69
	0.25	1.38±0.20±0.22	1.22±0.18±0.37
	0.35	0.69±0.12±0.14	1.12±0.19±0.23
	0.45	0.52±0.10±0.10	0.49±0.09±0.13
	0.55	0.12±0.02±0.05	0.17±0.03±0.05
	0.65	0.09±0.02±0.03	0.08±0.02±0.03
	0.75	0.14±0.04±0.03	
	0.85	0.033±0.010±0.015	
	0.95	0.016±0.005±0.008	
$K^{*+},\bar{K}^{*-}$	0.09	1.1±0.5	1.4±0.5
	0.18	0.9±0.4	0.9±0.5
	0.30	1.00±0.26	0.99±0.24
	0.42	0.73±0.21	0.33±0.14
	0.54	0.16±0.05	0.09±0.09
$K^{*0},\bar{K}^{*0}$	0.03	0.0±1.8	
	0.09	0.80±0.36	1.0±0.6
	0.18	0.95±0.21	1.2±0.4
	0.30	0.68±0.41	1.4±0.4
	0.42	0.73±0.35	1.4±0.9
ϕ	0.29	0.32±0.04	
	0.32		0.26±0.05
	0.48	0.08±0.02	
	0.53		0.02±0.01
	0.76	0.019±0.005	
	0.85		0.0003±0.0002

[a]The "$p,\bar{p}$" rates for $x=0.10$ are actually the $\bar{p}$ rates doubled.

is presumably a consequence of the decay of heavy particles and resonances. A light decay product like a pion tends to carry a small fraction of the parent momentum, while a heavy secondary (a kaon or proton, say) retains a large fraction. The behavior of the particle fractions in upsilon decay differs from the behavior in continuum annihilation. In upsilon decays the heavier particles, especially the protons, are more copious.

It would be interesting to study the charged-particle spectra over the complete momentum range, and to get

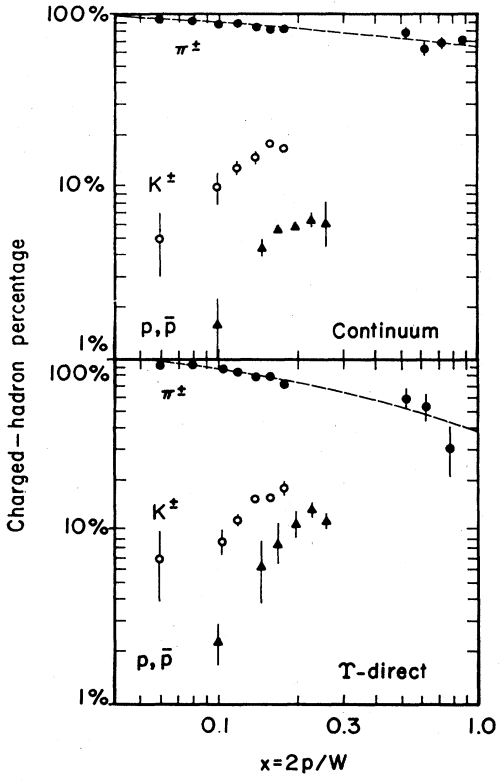

FIG. 10. Measured charged-hadron (π,K,p) fractions versus $x=2p/W$. Positive and negative charges are summed. The curves are drawn through the pion data are fits linear in $\ln x$. These fits are used in obtaining pion rates from total charge-hadron rates.

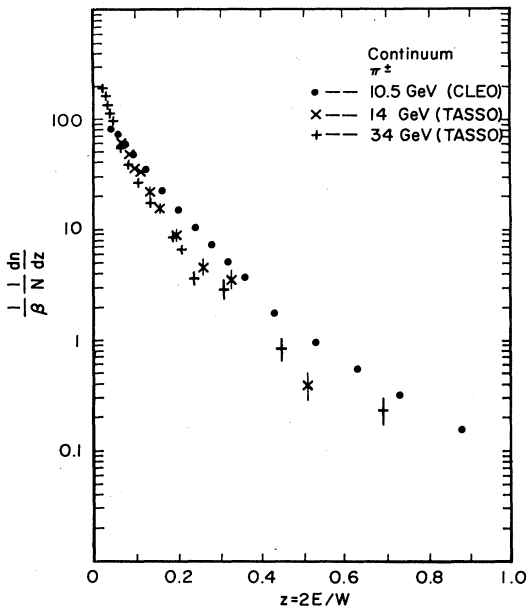

FIG. 11. Charged-pion spectra for continuum data derived by multiplying the spectra for all charged hadrons by the fits to the charged-pion fraction. The spectra are plotted in the form $(1/\beta N)dn/dz$ versus z, where z is the pion energy E divided by the beam energy $W/2$. The indicated errors are statistical only; systematic errors are given in Table IV. The data are compared with results from experiments at other center-of-mass energies (Ref. 15).

the total integrated yield for each particle. This is unfortunately not possible, because of the rather restricted momentum intervals within which the CLEO detector is able to identify charged hadrons. It is clear, however, from Fig. 10 that most charged hadrons are pions, especially at low momenta. One can therefore derive a reliable pion spectrum by starting with the momentum spectrum of all charged hadrons, without requiring identification, and multiplying by a smooth curve drawn through the pion fraction data of Fig. 10. In the following we will use pion data inferred in this way.

In order to compare our continuum particle spectra with data from other e^+e^- continuum experiments[15] we show them replotted (in Figs. 11—14) as $(1/\beta N)dn/dz$, where z is the fractional particle energy $2E/W$. It is customary when displaying continuum spectra to take out the dominant $1/s$ (that is, $1/W^2$) energy dependence of the cross sections by plotting $(s/\beta)d\sigma/dz$. Since we wish to make comparisons with upsilon spectra (Fig. 15), for which the cross section has a completely different value (which is not even directly measurable, because the beam energy resolution is wider than the resonance), we prefer to plot instead $(1/\beta\sigma_{\rm tot})d\sigma/dz$, or equivalently $(1/\beta N)dn/dz$. For continuum e^+e^- annihilation this is trivially related to $(s/\beta)d\sigma/dz$:

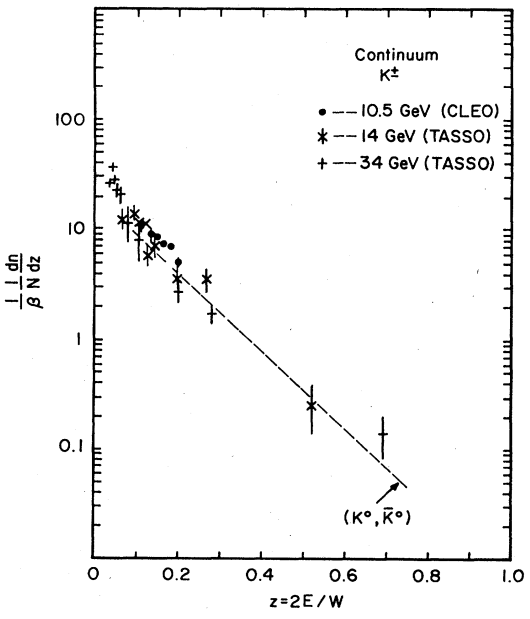

FIG. 12. Charged-kaon spectra for continuum data, plotted as $(1/\beta N)dn/dz$ versus $z=2E/W$. The indicated errors are statistical only; systematic errors are given in Table IV. The data are compared with results from experiments at other center-of-mass energies (Ref. 15). The dashed line shows for comparison the trend of our neutral-kaon data.

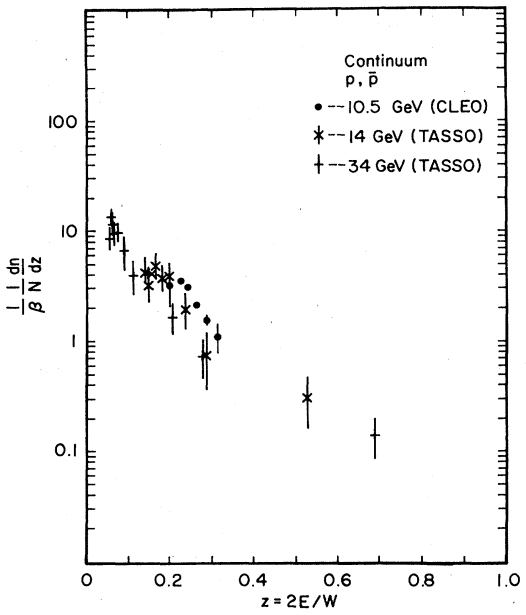

FIG. 13. Proton and antiproton spectra (summed) for continuum data, plotted as $(1/\beta N)dn/dz$ versus $z=2E/W$. The indicated errors are statistical only; systematic errors are given in Table IV. The data are compared with results from experiments at other center-of-mass energies (Ref. 15).

$$(1/\beta N)dn/dz=(3/4\pi\alpha^2R)(s/\beta)d\sigma/dz\ ,$$

where R is the ratio of the total cross sections for e^+e^- annihilation into hadrons and into muon pairs. The present CLEO continuum data are in satisfactory agreement with the data from the other experiments[15] (Figs. 11—13) if we make allowance for the experimental errors and for the apparent trend in the dependence on incident energy.

D. Spectrum shapes

Several different physical assumptions lead to conjectures about the form of the z (or energy) dependence of the single-particle inclusive spectra $(1/N)dn/dz$, independent of the details of the production mechanisms.

(1) Phase space. At least at threshold particle energies, one might expect the Lorentz-invariant spectrum $E\,d\sigma/d^3p$ to be independent of particle energy, that is, that $(1/N)dn/dz$ would be proportional to x (scaled particle momentum).

(2) Statistics. If the soft processes responsible for the production of the bulk of the final hadrons are essentially statistical in nature, one might expect a dependence on particle energy E like $e^{-E/kT}$, that is, $(1/N)dn/dz$ proportional to e^{-bz} with b to be determined from the data. The scaling hypothesis would suggest that b should be independent of center-of-mass energy. A significant contribution to the lighter particle yields, especially at lower energies, are the products of the strong decays of high-mass particles and resonances; heavy particles are likely to have spectra which more closely reflect the parent distributions.

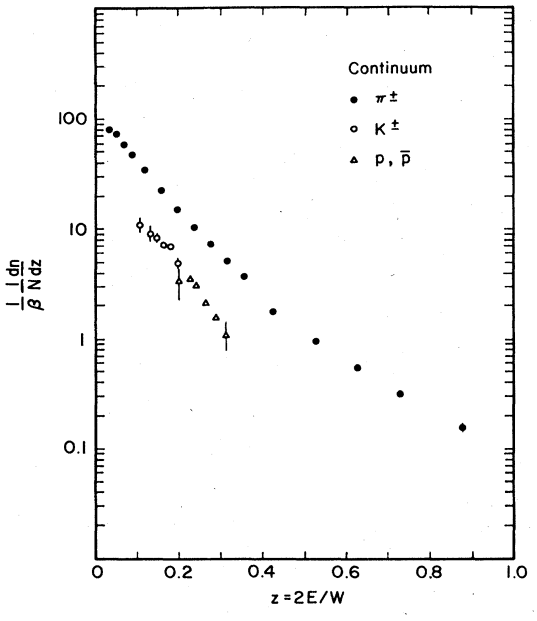

FIG. 14. Comparison of pion, kaon, and proton inclusive spectra from continuum annihilations, plotted as $(1/\beta N)dn/dz$ versus $z=2E/W$. The indicated errors are statistical only; systematic errors are given in Table IV.

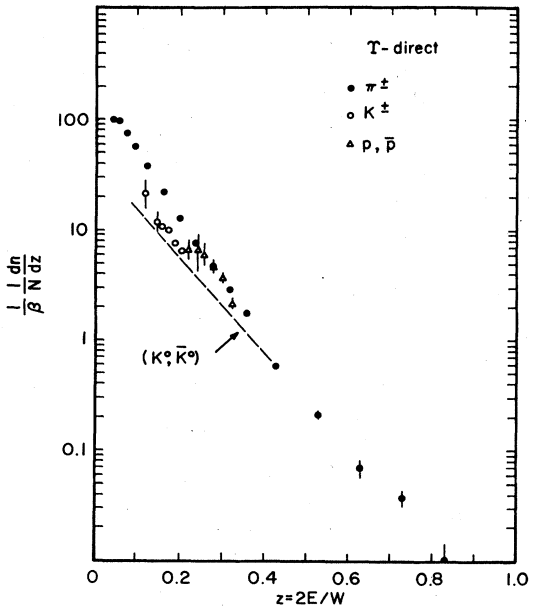

FIG. 15. Comparison of pion, kaon, and proton inclusive spectra from upsilon strong decays, plotted as $(1/\beta N)dn/dz$ versus $z=2E/W$. The indicated errors are statistical only; systematic errors are given in Table IV. The dashed line shows for comparison the trend of our neutral-kaon data.

(3) High-energy limit. The z spectrum must of course go to zero at the kinematic limit $z \approx 1$ (that is, $E = W/2$). Various theoretical ideas[16] suggest a power-law behavior $(1-z)^2$ near $z=1$, although there is no reason to expect such a form to persist to much lower z.

Our charged-pion data are our most accurate and cover the widest momentum range. They are therefore well suited for testing the functional form of the z spectrum. We can test the hypothesis that the continuum spectrum has the form

$$(1/N)dn/dz = A(x/z)e^{-bz} = \beta A e^{-bz} ,$$

which incorporates conjectures (1) and (2) above, by looking in Figs. 14 and 15 for a straight line in $\log(1/\beta N)dn/dz$ versus z. The agreement is good up to $z=0.5$, although at the larger z values the observed continuum spectrum becomes flatter. Table V shows fits for A and b obtained for all charged particle types, for continuum and upsilon data sets. Also tabulated are the integrals over the best fit functions:

$$\bar{n} = \int (1/N)(dn/dz)dz = \int \beta A e^{-bz} dz ,$$

the mean number of the specified type of hadrons per event. Possible deviations from the fit at higher z do not significantly affect the integrals. Because we identify charged kaons and protons only in narrow momentum ranges, the slopes of the K and p spectra are poorly determined by the data. Therefore, in calculating the corresponding A and $\bar{n}$ parameters for Table V (and Table VI), we have fixed the slopes b to be the same as measured for K^0 and Λ, respectively. Note that although the A and b parameters may be approximately independent of beam energy, the β factor implies that the rate $(1/N)dn/dz$ cannot scale for z near threshold and that the integral $\bar{n}$ will depend on the center-of-mass energy.

A check for power-law behavior near $z=1$ is made difficult by the fact that our charged-particle momentum resolution (derived from Monte Carlo simulation) caused the rms spreading in z to increase quadratically, essentially as $\delta z = 0.04z^2$.

V. NEUTRAL HADRONS DECAYING INTO PHOTONS: π^0 AND η

A. Identification of π^0

Neutral pions were recognized by their decay into photon pairs. In order to have the best energy resolution we used only the large-angle shower calorimetry covering the polar angle range $45° < \theta < 135°$. Candidate photon showers were required to have no associated charged track in the main drift chamber, and a measured pulse height corresponding to at least 300 MeV. Figure 16 shows a typical calculated invariant mass spectrum of pairs of photon showers. The peak at about 135 MeV corresponding to the π^0 is evident above the combinatoric background of randomly paired photons. The π^0 signal was extracted by fitting the mass distribution to a Gaussian peak plus a polynomial background. For π^0 energies cor-

TABLE V. Results from fits to $(1/N)dn/dz = \beta A e^{-bz}$. Statistical and systematic errors are added in quadrature.

	Continuum			Upsilon		
Hadron	A	b	$\bar{n}$ [a]	A	b	$\bar{n}$ [a]
π^+,π^-	124±6	10.2±0.1	8.3±0.4	206±10	13.7±0.1	8.7±0.4
K^+,K^-	28±4	(8.0)	1.3±0.2	50±7	(9.9)	1.4±0.2
$p,\bar{p}$	30±4	(9.4)	0.40±0.06	130±20	(12.1)	0.60±0.09
π^0	36±11	8.8±0.9	3.0±0.7	117±47	13.3±1.1	5.2±1.8
$K^0,\bar{K}^0$	20±3	8.0±0.2	0.92±0.12	39±5	9.9±0.2	1.05±0.13
$\Lambda,\bar{\Lambda}$	7.2±2.3	9.4±0.8	0.066±0.010	69±14	12.1±0.5	0.19±0.02
$\Xi^-,\bar{\Xi}^+$	1.1±0.8	10.0±1.8	0.005±0.001	5±5	10.7±2.3	0.016±0.004
ρ^0	14±4	7.2±0.5	0.50±0.09	32±11	8.9±0.7	0.57±0.14
K^{*+},K^{*-}	24±6	8.5±0.5	0.45±0.08	63±26	11.2±0.9	0.42±0.15
$K^{*0},\bar{K}^{*0}$	7.2±4.6	5.5±2.4	0.38±0.09	6.0±5.4	3.1±2.4	0.8±0.3
ϕ	2.6±1.2	6.4±1.0	0.08±0.02	84±32	14.3±0.7	0.15±0.05
All[b]			13.4±0.8			16.5±1.9
Charged[c]			10.0±0.5			10.7±0.5
Vector[d]			2.9±0.4			3.6±0.7
Strange[e]			2.3±0.3			2.8±0.4
Baryon[f]			0.80±0.12			1.20±0.18

[a]The mean number of specified particles per event is defined by $\bar{n} = \int D_g^h(z)dz$, with the lower z limit given by $2m_h/W$, where $W = 10.49$ GeV for the continuum data and $W = M_\Upsilon = 9.46$ GeV for the upsilon data.

[b]All $= \pi^+ + \pi^- + \pi^0 + K^+ + K^- + 2(p + \bar{p})$.

[c]Charged $= \pi^+ + \pi^- + K^+ + K^- + p + \bar{p}$.

[d]Vector $= 4\rho^0 + K^{*+} + K^{*-} + K^{*0} + \bar{K}^{*0} + \phi$.

[e]Strange $= K^+ + K^- + K^0 + \bar{K}^0 + 2(\Lambda + \bar{\Lambda})$.

[f]Baryon $= 2(p + \bar{p})$.

TABLE VI. Gluon and quark fragmentation functions,[a] expressed as $D(z)=\beta A\, e^{-bz}$. Statistical and systematic errors are added in quadrature.

Hadron	A_q	b_q	$\bar{n}_q$[b]	A_g	b_g	$\bar{n}_g$[b]
π^+,π^-	62±3	10.2±0.1	4.0±0.2	120±6	12.1±0.1	6.1±0.3
K^+,K^-	14±2	(8.0)	0.59±0.10	22±3	(8.3)	0.86±0.13
$p,\bar{p}$	15±2	(9.4)	0.20±0.04	68±11	(10.5)	0.51±0.08
π^0	18±4	8.8±0.9	1.4±0.3	67±27	11.7±1.0	3.6±1.2
$K^0,\bar{K}^0$	9.9±1.2	8.0±0.4	0.42±0.05	17.7±2.5	8.3±0.2	0.69±0.08
$\Lambda,\bar{\Lambda}$	3.6±1.3	9.4±0.8	0.026±0.004	36±7	10.5±0.5	0.17±0.02
$\Xi^-,\bar{\Xi}^+$	0.6±0.4	10.0±1.8	0.002±0.001	2.4±2.4	9.1±2.0	0.014±0.004
ρ^0	7.0±2.0	7.2±0.5	0.22±0.04	13±4	7.3±0.6	0.39±0.10
K^{*+},K^{*-}	12±3	8.5±0.5	0.19±0.03	31±13	9.6±0.9	0.34±0.12
$K^{*0},\bar{K}^{*0}$	3.6±2.3	5.5±2.4	0.21±0.05	1.2±1.0	1.5±1.2	0.3±0.1
ϕ	1.3±0.6	6.4±1.0	0.035±0.007	51±19	12.7±0.6	0.15±0.05

[a]The fragmentation functions are defined in terms of our continuum and upsilon data:

$$(1/N_c)dn_c^h/dz = 2D_q^h(z)\ ,$$

$$(1/N_\Upsilon)dn_\Upsilon^h/dz = 3\int_z^1 D_g^h(u)G(z/u)du/u\ .$$

[b]The integral is defined by $\bar{n}_g^h = \int D_g^h(z)dz$, with the lower z limit given by $2m_h/M_\Upsilon$.

responding to $x>0.5$ it is not possible to make a reliable separation of signal from background.

It is clear from the two-photon mass spectrum (Fig. 16) that eta mesons are also produced. Because of the limited statistics and the large backgrounds, it is not possible to get reliable η cross sections from our data.

B. Calculation of the inclusive rate

The calculation of the π^0 yields for continuum and upsilon direct was carried out in a way similar to the calculation of the charged hadron yields described above. One difference, however, concerned the correction for acceptance. There is no reliable way to calculate the efficiency for reconstruction from the actual data; we had to rely on Monte Carlo simulation. So rather than using the method described for charged hadrons, we determined the combined effect of event acceptance and π^0 decay reconstruction efficiency in a single calculation (separately for continuum and upsilon) with the acceptance binned in the x of the pion. The program simulated the raw data for entire events, including hits in the proportional tubes of the shower calorimeter, which were then reconstructed into photon showers and π^0 candidates by the standard analysis used on real data. In this way all correlations between x and the acceptance were accounted for, but the result becomes more dependent on the Monte Carlo model for particle production in e^+e^- annihilation. The parameters of the model were of course tuned so that the simulated "observed" distributions matched the actually observed distributions as closely as possible. Nevertheless, the systematic error (typically 20%) was larger than in the method used for charged hadrons. Because of the restricted geometrical aperture and the cuts used to suppress background, the π^0 acceptance was rather low (see Table III).

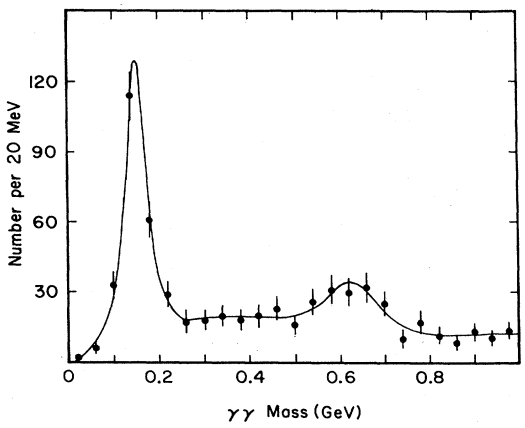

FIG. 16. Typical mass spectrum of detected photon pairs.

The x and z spectra for neutral pions produced in the continuum and in direct upsilon decays are shown in Figs. 17 and 18 and in Table IV. The continuum data are compatible with results from experiments at other center-of-mass energies.[17] Table V shows the results of fits to the form

$$(1/N)dn/dz = \beta A e^{-bz}\ .$$

VI. HADRONS WITH DETECTABLE DECAY LENGTHS: K^0, Λ, AND Ξ^-

A. K_S^0 and Λ identification

We reconstructed K_S^0 and Λ (or $\bar{\Lambda}$) candidates from their decay tracks in the cylindrical drift chamber. A kaon (lambda) candidate was a positive-negative track pair with an extrapolated intersection at least 5 mm (8 mm) from the primary event vertex and a net momentum vector extrapolating back to the event vertex. Each of the two tracks had at least 100-MeV/c momentum and the

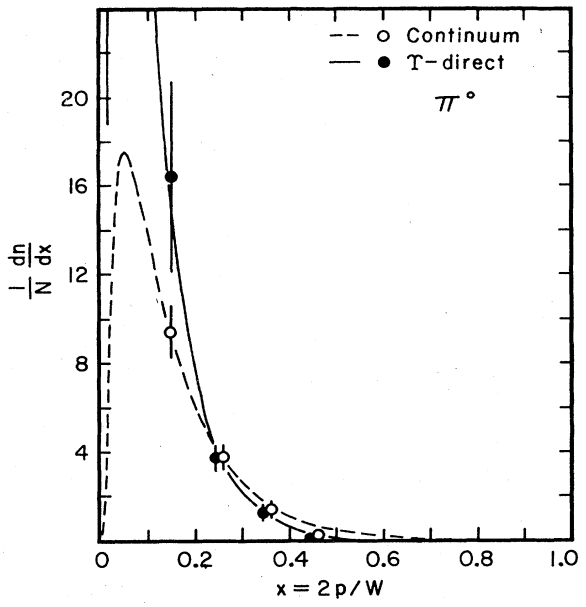

FIG. 17. Measured inclusive spectra for neutral pions from continuum data (open circles) and upsilon strong decays (closed circles), plotted as mean number per event per unit x, where $x=2p/W$. The indicated errors are statistical only; systematic errors are given in Table IV. The curves show the fits described in the text.

combination had to be above 450 MeV/c, since below these momenta our acceptance is poor. Different hypotheses for the masses of the charged tracks were used. We rejected any pair consistent with photon conversion to e^+e^-; we accepted a pair as a K_S^0 decay if the $\pi^+\pi^-$ invariant mass (Fig. 19) was within 20 MeV of the kaon mass; and any $p\pi^-$ ($\bar{p}\pi^+$) candidate within 5 MeV of the lambda mass was taken to be a Λ ($\bar{\Lambda}$). Ambiguous cases were rejected.

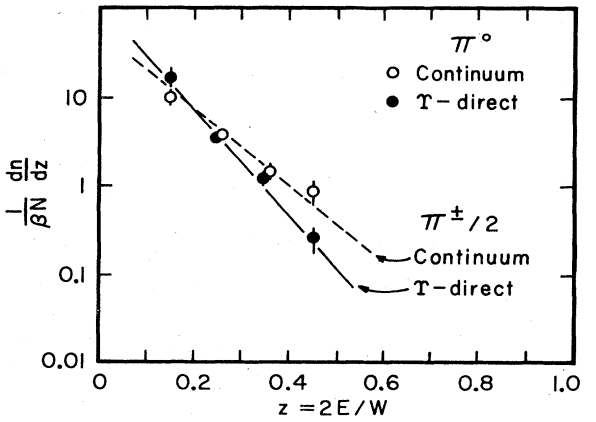

FIG. 18. Neutral-pion inclusive spectra plotted as $(1/\beta N)dn/dz$ versus $z=2E/W$, for continuum data and upsilon strong decays. The indicated errors are statistical only; systematic errors are given in Table IV. For comparison the curves show our charged-pion spectrum ($\pi^+ + \pi^-$), multiplied by one half.

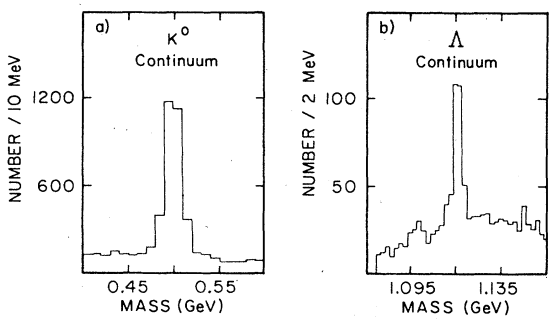

FIG. 19. Sample effective-mass spectra for opposite-sign charged-particle pairs which form a secondary vertex separate from the main event vertex: (a) assuming pion masses, (b) assuming a nucleon mass and a pion mass. The peaks correspond to (a) $K_S^0 \to \pi^+\pi^-$ and (b) $\Lambda \to p\pi^-$ (and charge conjugate, summed).

We fitted each mass plot to the sum of a Gaussian signal and a smoothly varying background to determine the number of background candidates within the mass cuts. The x spectrum of the background, determined from the data in sidebands on either side of the mass peak, was subtracted from the x distribution of the data within the peak cut to obtain the x spectrum of the kaon or lambda signal.

B. Identification of Ξ^-

Xi reconstruction began with an identified Λ ($\bar{\Lambda}$) candidate combined with any charged track having momentum above 100 MeV/c and having a distance of closest approach to the beam axis greater than 1.5 mm. The distance from the beam line to the common vertex, if any, of the lambda and the charged track had to be between 5 mm and the radius of the Λ decay vertex, and the net momentum had to point to the primary event vertex within 10°. We also required that the apparent proper lifetime of the Ξ candidate be greater than 0.1 times its mean life. Since we used looser requirements on the Λ from Ξ decay than in our Λ inclusive measurement, our Ξ efficiency was actually higher than our Λ efficiency (Table III).

Figure 20 shows distributions in the calculated mass of the Ξ candidates. There is a clear peak at the Ξ mass. We determined the background under the peak by repeating the analysis for the wrong sign combinations, $\Lambda\pi^+$ and $\bar{\Lambda}\pi^-$.

C. The inclusive spectra

The calculation of the yields of K^0, Λ, and Ξ^- for continuum and upsilon strong decays were carried out in a way similar to the calculation of the neutral pion yields described above. That is, we determined the combined effect of event acceptance and neutral decay reconstruction efficiency in a single calculation (separately for continuum and upsilon) with the acceptance binned in the x of the neutral vee. The systematic error of 12% reflects the dependence on the Monte Carlo model.

Table III shows the acceptances for neutral kaons,

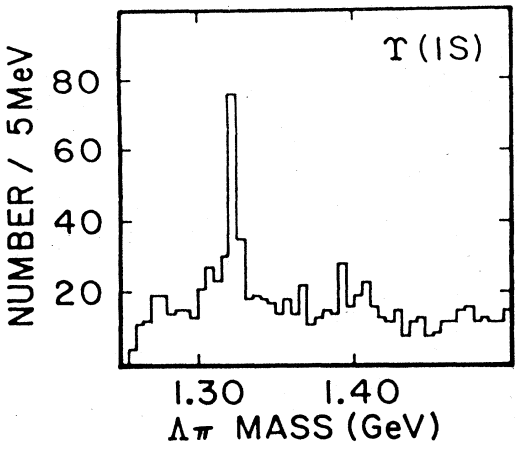

FIG. 20. Sample effective-mass spectrum for lambda-pion combinations which form a secondary vertex separate from the main event vertex. The peak corresponds to the decay $\Xi^- \to \Lambda\pi^-$ (plus charge conjugate).

lambdas, and charged xi's as functions of x. Included in the acceptance is the effect of undetected decay modes, such as $K_S^0 \to \pi^0\pi^0$, $K_L^0 \to$ anything, $\Lambda \to n\pi^0$.

In Figs. 21–25 we plot the x and z spectra of the neutral kaons, lambdas, and charged xi hyperons (see also Table IV). In each case the plotted rate includes particle and antiparticle summed. The hyperon and antihyperon rates are equal within errors. The agreement between our

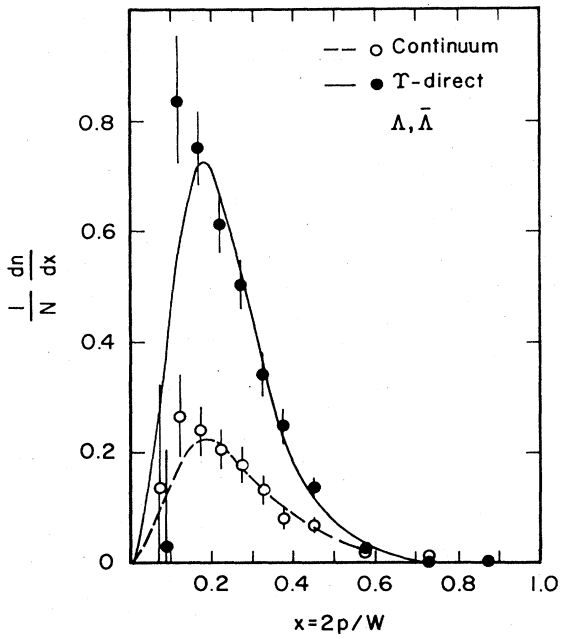

FIG. 22. Inclusive lambda spectra in particles per event per unit $x = 2p/W$ (Λ and $\overline{\Lambda}$, summed) from continuum data (open circles) and upsilon strong decays (closed circles). The indicated errors are statistical only; systematic errors are given in Table IV. The curves show the fits described in the text.

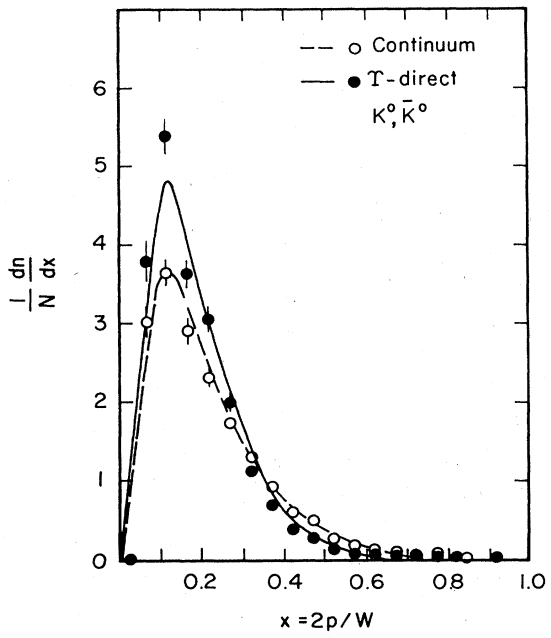

FIG. 21. Inclusive neutral-kaon spectra in particles per event per unit $x = 2p/W$ (K^+ and K^-, summed) from continuum data (open circles) and upsilon strong decays (closed circles). The indicated errors are statistical only; systematic errors are given in Table IV. The curves show the fits described in the text.

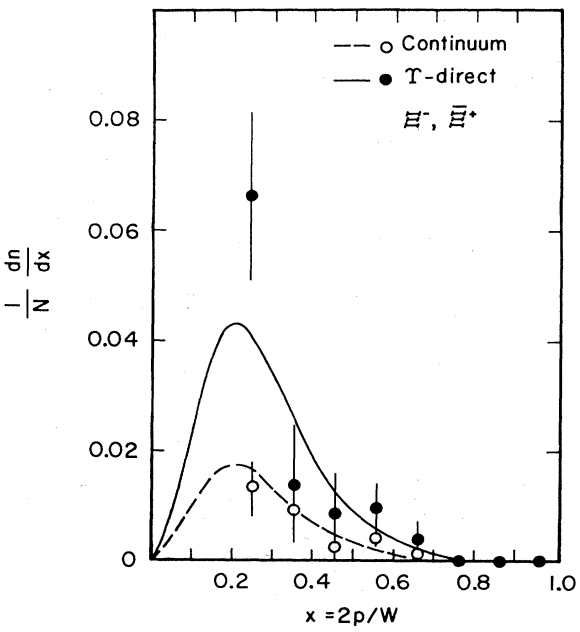

FIG. 23. Inclusive Ξ^- spectra in particles per event per unit $x = 2p/W$ (Ξ^- and $\overline{\Xi}^+$, summed) from continuum data (open circles) and upsilon strong decays (closed circles). The indicated errors are statistical only; systematic errors are given in Table IV. The curves show the fits described in the text.

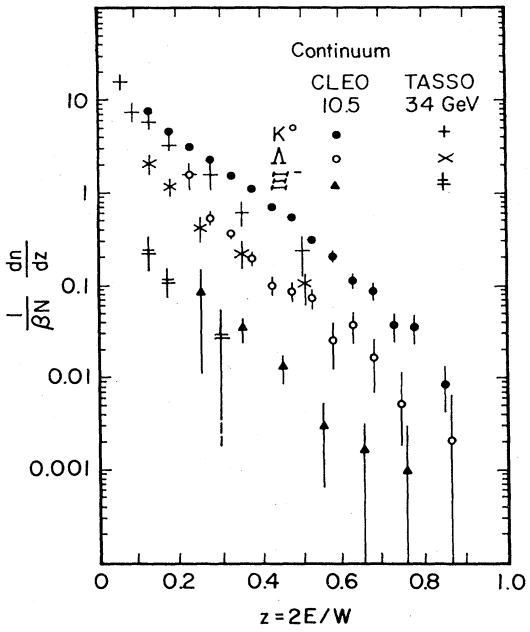

FIG. 24. Inclusive K^0, Λ, and Ξ^- spectra (particle and antiparticle, summed) from continuum data, plotted as $(1/\beta N)dn/dz$ versus $z=2E/W$. The data from this experiment are compared with data from experiments at other center-of-mass energies (Ref. 18). The indicated errors are statistical only; systematic errors are given in Table IV.

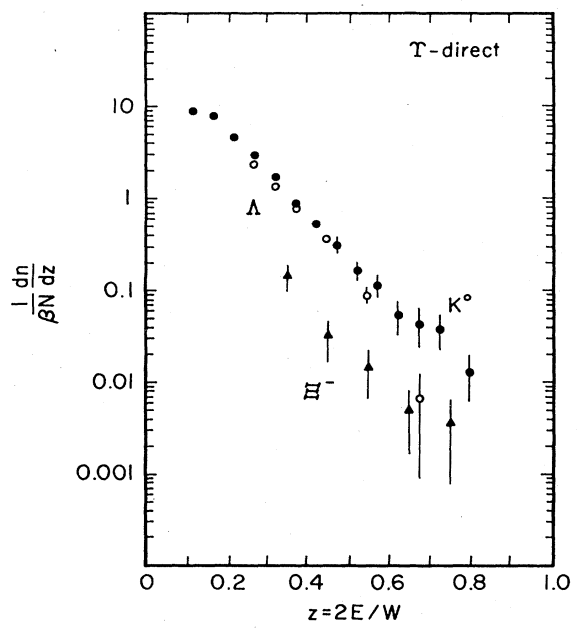

FIG. 25. Inclusive K^0, Λ, and Ξ^- spectra (particle and antiparticle, summed) from upsilon strong decays, plotted as $(1/\beta N)dn/dz$ versus $z=2E/W$. The indicated errors are statistical only; systematic errors are given in Table IV.

continuum K^0 data and data from other experiments[18] is satisfactory within the measurement errors and the deviations expected from scale breaking and the range of incident energies.

We have fit the spectra in z to the functional form

$$(1/N)dn/dz = \beta A e^{-bz},$$

discussed in Sec. IV C. The resulting A and b parameters are given in Table V along with the integrated multiplicities implied by the fits.

D. Lambda polarization

The angular distribution of the Λ decay is sensitive to the polarization of the Λ. Unfortunately, the decay angle also affects the efficiency for detection. In Fig. 26 we plot the observed distributions in the cosine of the angle of the decay p or $\bar{p}$ with respect to the normal $(\mathbf{p}_{e+}\times\mathbf{p}_\Lambda)$ to the production plane, measured in the Λ rest frame. No correction for acceptance was made; instead, the curves show the Monte Carlo distributions obtained by assuming no polarization and simulating the detector acceptance. The data for both the continuum and the upsilon are completely consistent with no polarization.

In the Lund string model[19] of hadronization in e^+e^- annihilation the Λ spin comes from the strange quark, which is created with no preferred orientation; and therefore no Λ polarization is expected.

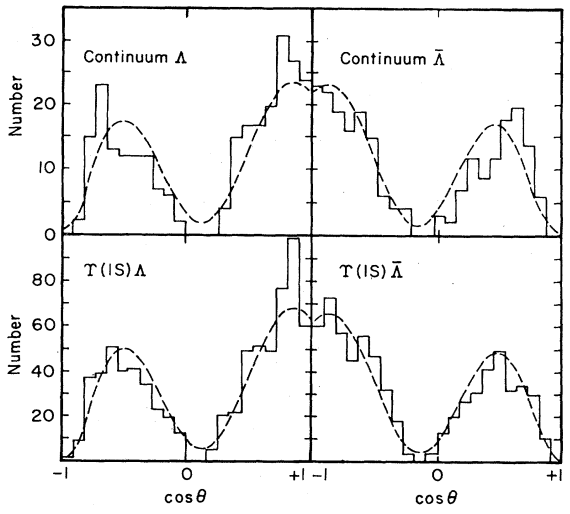

FIG. 26. Uncorrected observed distribution of angles in the decay of Λ and $\bar{\Lambda}$ produced in the continuum and in upsilon strong decays. The angle plotted is the angle between the decay p or $\bar{p}$ and the normal to the production plane $(\mathbf{p}_{e+}\times\mathbf{p}_\Lambda)$, measured in the lambda rest frame. The curves are the prediction of a Monte Carlo simulation taking into account the detector acceptance but assuming no polarization of the lambdas.

VII. STRONGLY DECAYING HADRONS: ρ^0, f^0, K^*, AND ϕ

A. Neutral rho and f mesons

We observe a ρ^0 signal by reconstructing the effective mass of all pairs of oppositely charged tracks, assuming they are pions. To minimize the contribution from K_S^0 and Λ decays we rejected tracks which did not extrapolate to within 6 mm of the beam line, and to reduce other backgrounds we required the momenta to be greater than 200 MeV/c. The resulting dipion mass spectrum (Fig. 27) shows a peak at the rho mass. There is also evidence for production of the $f(1270)$ (Fig. 28). To extract the ρ^0 signal we made a fit in each x interval to a Breit-Wigner signal, plus a polynomial background, plus contributions from $K^{*0}\to K^+\pi^-$ (and charge conjugate), with the kaon treated as a pion, and from $\omega\to\pi^+\pi^-\pi^0$, the π^0 not detected. The shapes of the mass spectra for the ρ, K^*, and ω contributions were obtained from a Monte Carlo calculation; only the magnitudes were varied in the fit. The whole analysis procedure was repeated in Monte Carlo simulation to get the acceptance as a function of x (Table III). The resulting spectra in x and z are plotted in Figs. 29–31 (along with continuum data at higher energy[20]) and are listed in Table VI.

Our Monte Carlo program does not generate tensor mesons. If we assume that the f^0 acceptance is the same as for the ρ^0, we obtain f^0 production rates per event of $0.085\pm0.017\pm0.018$ in the continuum ($x>0.2$) and $0.011\pm0.007\pm0.003$ in upsilon decays ($x>0.5$). The x limits are imposed because of our inability to extract the f^0 signal from background at lower momenta.

B. $K^*(890)$

We observe the K^{*+} (and charge conjugate) through the decay sequence $K^{*+}\to K_S^0\pi^+$ followed by $K_S^0\to\pi^+\pi^-$. Each reconstructed K_S^0 (see Sec. VI) was paired with each charged track having momenta above 200 MeV/c and not identified as being other than a pion. The $K^0\pi$ effective-mass plot (Fig. 32) shows a peak at the K^* mass. To extract the number of K^* observed we fit the mass distribution with a Breit-Wigner on a fourth-order polynomial background. The shape of the background was fit to the uncorrelated mass plot; only the overall scale was allowed to vary in the final fit. The fitted position and width of the Breit Wigner give

$$M(K^{*+})=892\pm2\ \text{MeV},\quad \Gamma(K^{*+})=61\pm4\ \text{MeV},$$

in close agreement with the known values.[21] The fit procedure was used for each of the bins in x.

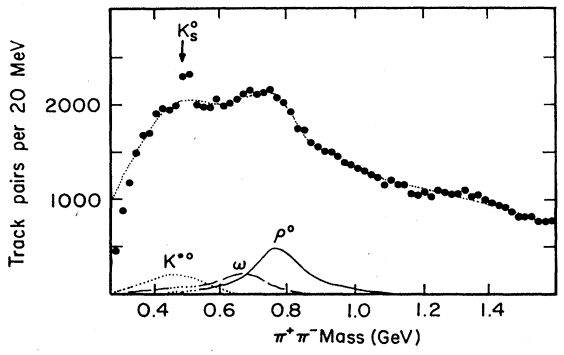

FIG. 27. Sample effective-mass spectrum of opposite-charge pairs of tracks taken to be pions. The curves at the bottom show the fitted contributions of $K^{*0}\to K^\pm\pi^\mp$ (misidentifying the kaon as a pion), $\omega\to\pi^+\pi^-\pi^0$ (with the π^0 missed), and $\rho^0\to\pi^+\pi^-$. The mass region near 0.5 GeV is dominated by $K_S^0\to\pi^+\pi^-$ and is omitted from the fit.

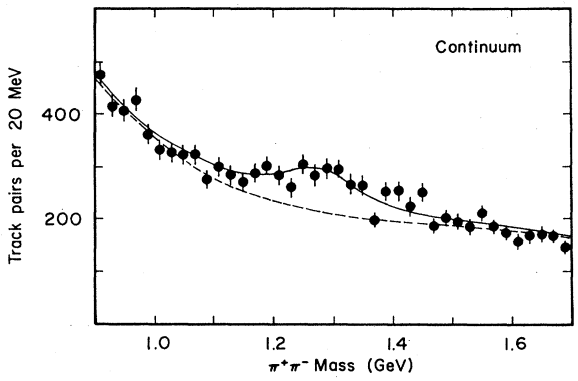

FIG. 28. Continuum $\pi^+\pi^-$ mass spectrum in the high-mass region, showing a fit which includes a contribution from $f^0(1270)\to\pi^+\pi^-$.

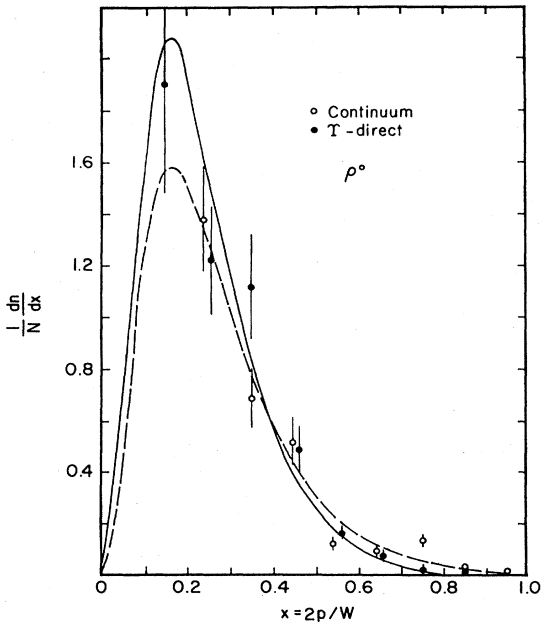

FIG. 29. Inclusive x spectra for ρ^0 from continuum data (open circles) and from upsilon strong decays (closed circles). The indicated errors are statistical only; systematic errors are given in Table IV. The curves show the fits described in the text.

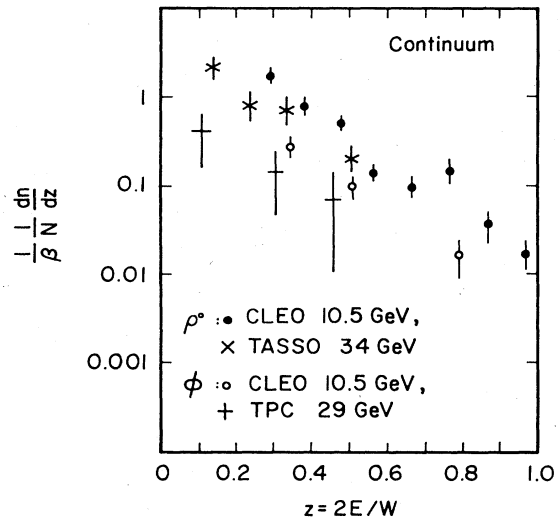

FIG. 30. Comparison of inclusive z spectra for ρ^0 and ϕ from continuum data. The indicated errors are statistical only; systematic errors are given in Table IV. Data from experiments at other center-of-mass energies are included for comparison (Refs. 20 and 22).

The efficiency for K^{*+} detection was obtained by Monte Carlo simulation, processing the events with the same techniques by which the K^* signal was obtained in the real data. Isospin invariance implies that the total number of K^{*+} produced is $\frac{9}{2}$ the number observable in the $(\pi^+\pi^-)\pi^+$ topology; this factor is included in our final corrected rates. The results for the x and z spectra and integrated rates are given in Figs. 33—35 and in Tables IV and V.

The K^{*0} (and charged conjugate) was recognized

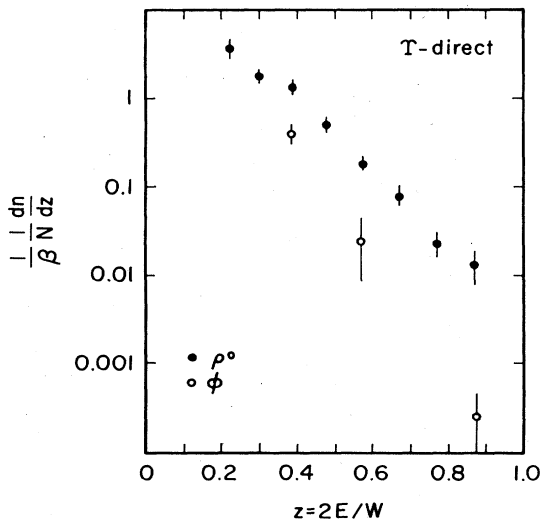

FIG. 31. Comparison of inclusive z spectra for ρ and ϕ from upsilon strong decays. The indicated errors are statistical only; systematic errors are given in Table IV.

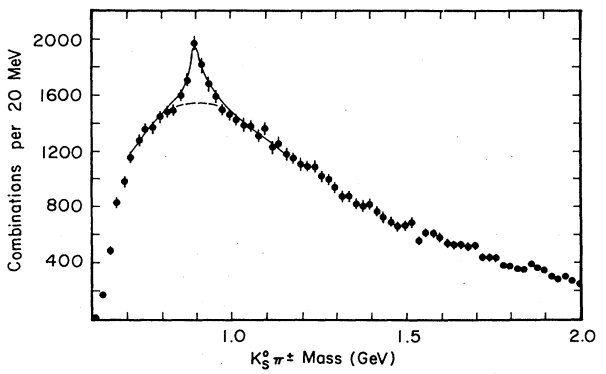

FIG. 32. Typical effective-mass spectrum of K^0_S-plus-charged-pion combinations. The peak at about 890 MeV is interpreted as the decay $K^{*+}\to K^0_S\pi^+$ and charge conjugate. The curves show the fit to signal and background.

through its decay $K^{*0}\to K^+\pi^-$. That is, we paired charged kaons identified by time of flight or dE/dx with all oppositely charged tracks which were not identified as being other than pions, and plotted the distribution of effective masses (Fig. 36). The peak at about 890 MeV was taken to be the K^{*0} (and $\overline{K}^{*0}$). The number of observed K^* was obtained by fitting the mass spectrum to a Breit-Wigner plus a polynomial background, for each bin in x and for the continuum and upsilon data sets. The acceptance was determined by Monte Carlo simulation, except that the efficiency for kaon identification in the time-of-flight and dE/dx systems was taken from the data, as explained in Sec. IV.

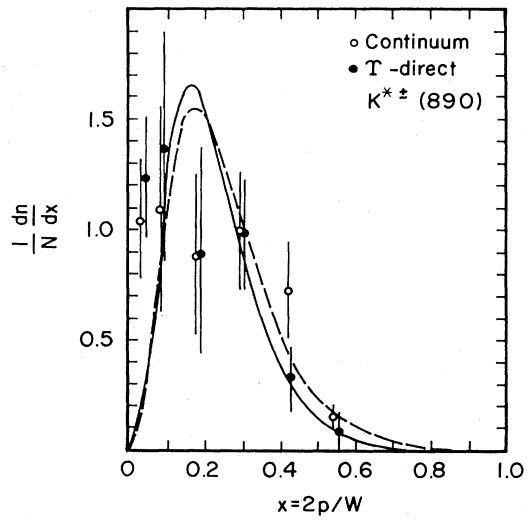

FIG. 33. Inclusive x spectra for $K^{*\pm}$ from continuum data (open circles) and from upsilon strong decays (closed circles). The indicated errors are statistical only; systematic errors are given in Table IV. The curves show the fits described in the text.

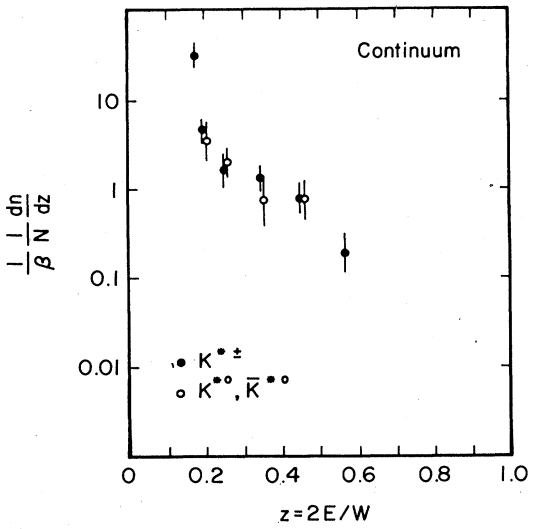

FIG. 34. Comparison of inclusive z spectra for charged and neutral $K^*(890)$ from continuum data. The indicated errors are statistical only; systematic errors are given in Table IV.

C. The phi meson

The phi meson was identified in its dominant decay mode, $\phi \to K^+K^-$. We used two different methods. In the first, we calculated the two-kaon effective mass of all oppositely charged pairs of tracks having momenta over 300 MeV/c and not identified as other than kaons. The mass spectrum for each of three x bins [Fig. 37(a)] shows a peak at the phi mass. In the second method, we required the positive identification of at least one of the two kaons, thus restricting it to be in the momentum range 0.45—1.0 GeV/c. The mass plot [Fig. 37(b)] shows a cleaner phi peak but fewer events. The fit of all the data to a Gaussian plus a polynomial background gave

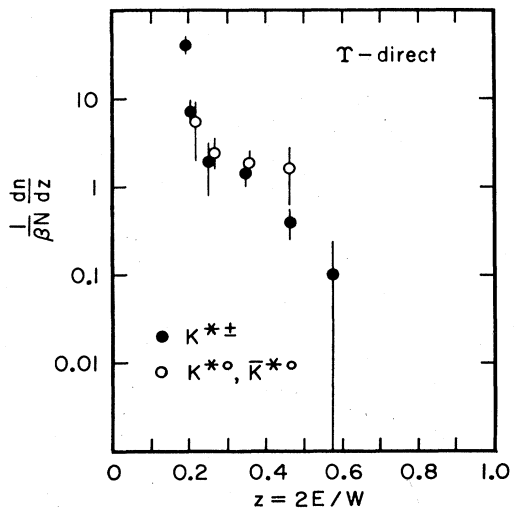

FIG. 35. Comparison of inclusive z spectra for charged and neutral $K^*(890)$ from upsilon strong decays. The indicated errors are statistical only; systematic errors are given in Table IV.

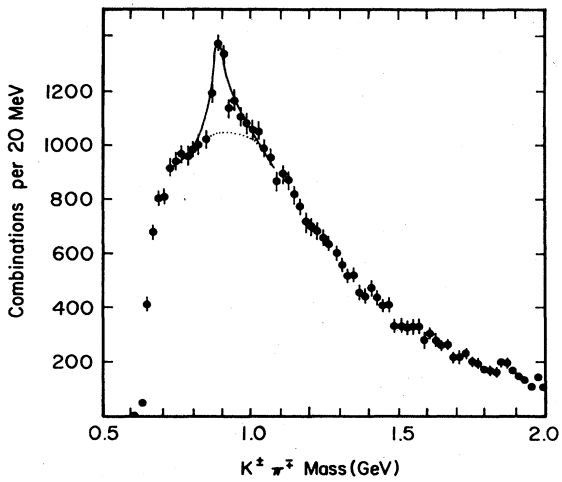

FIG. 36. Typical effective-mass spectrum of oppositely charged kaon-pion pairs. The peak at about 890 MeV is interpreted as the decay $K^{*0} \to K^+\pi^-$ and charge conjugate. The curves show the fit to signal and background.

$$M(\phi) = 1018.9 \pm 1 \text{ MeV}$$

in agreement with the accepted value,[21] and an rms width of 6±1 MeV, consistent with our resolution.

For each x bin the acceptance was calculated by Monte Carlo simulation of the ϕ production, the performance of the detector, and the analysis procedure. The corrected rates also take account of the other decay modes. For the second method, in which we required identification of one

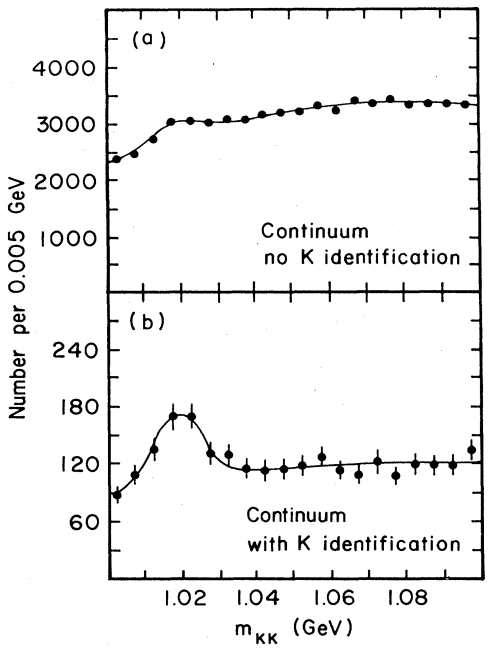

FIG. 37. Typical effective-mass spectra of oppositely charged kaon pairs: (a) all tracks assumed to be kaons, (b) identified kaons only. The peak at about 1020 MeV is interpreted as the decay $\phi \to K^+K^-$. The curves show fits to signal plus background.

of the kaons, the data were also corrected for the efficiency and aperture of the time of flight system and the dE/dx chambers. The rates derived by the two methods agree where they overlap, and the averaged spectra are shown in Figs. 30, 31, and 38 along with continuum data at higher energy.[22]

VIII. COMPARISONS OF PARTICLE SPECTRA

A. Charged vs neutral

The hadronization of the primary quarks and gluons is expected to be isospin invariant. That is, production of the various charge states of an isospin multiplet should be equal: $\pi^+=\pi^-=\pi^0$ and charged K=neutral K. Deviations from isospin symmetry in the final state can, however, be expected from weak decays of produced hadrons (the D mesons, for instance) or from strong decays in cases (such as the ϕ) where branching ratios are sensitive to small electromagnetic mass differences. If all other sources of kaon production were isospin symmetric, our measured ϕ inclusive rates would lead to a charged/neutral kaon ratio of about 1.02 in the continuum and 1.05 on the upsilon. More important may be the fact that the electromagnetic creation of the primary quark pair in continuum annihilation is not necessarily isospin symmetric.

Figure 18 shows the measured π^0 rate to be consistent with the average of the π^+ and π^- rates, although in view of the uncertainties (typically 30% in the ratio of neutral and charged rates) the test is not very significant. The comparison of charged and neutral kaon yields is possible only in the 0.5—1.0-GeV/c range available for charged kaon identification (see Figs. 12 and 15). The rates are consistent with being equal, although again the systematic errors allow for some deviation.

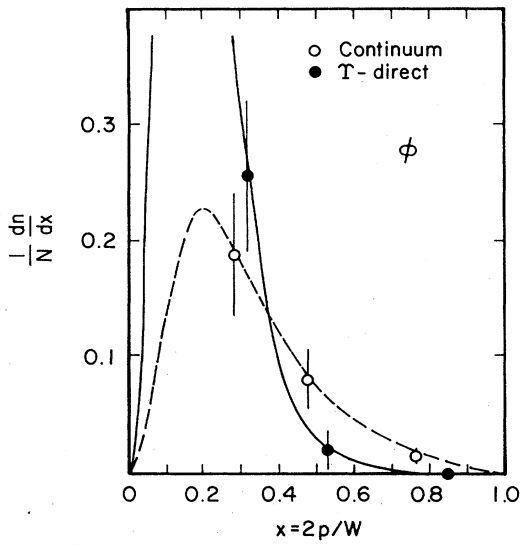

FIG. 38. Inclusive x spectra for ϕ from continuum data (open circles) and from upsilon strong decays (closed circles). The indicated errors are statistical only; systematic errors are given in Table IV. The curves show the fits described in the text.

B. Quark and gluon fragmentation functions

The production of hadron final states by e^+e^- annihilation in the nonresonant continuum is commonly assumed to take place in two stages: the creation of quark-antiquark pair by the virtual photon, and the subsequent hadronization of the quarks to form collimated jets of particles. If we think of each quark as fragmenting independently into hadrons,[13,23] the scaled energy spectrum for a particular type of hadron h should then be twice the probability distribution $D_q^h(z)$ for a quark q to produce a hadron h of fractional energy $z=E/E_q$:

$$(1/N_c)dn_c^h/dz=2D_q^h(z)\ .$$

The fragmentation functions $D_q^h(z)$ which we measure are of course averaged over the flavors u,d,s,c of the quarks produced in the continuum, with weights proportional to their charges squared, 4,1,1,4.

The direct hadronic decay of the upsilon is assumed to proceed through a three-gluon intermediate state, hadronizing into three jets. The comparison of particle spectra in the continuum and from the upsilon should therefore (in the context of the independent fragmentation picture) be a comparison of fragmentation functions in quark and gluon jets. The comparison cannot be made directly, however. At the center-of-mass energies we are concerned with here the jets tend to overlap, especially in the three gluon decay, and we do not attempt to separate them. Because the three jets in upsilon decay can share the total energy in various ways, they are not directly comparable to monoenergetic quark jets of energy equal to half the upsilon mass. We can take account of this by making use of the QCD prediction for the energy distribution $G(2E_g/W)$ of gluons in three-gluon decays, and extracting a gluon fragmentation function D_g^h. We make the following assumptions.

(1) Hadron fragmentation functions in gluon jets can be approximated by the same functional form which we use to characterize quark jets, although perhaps with different A and b parameters;

$$D_g^h(u)=\beta_u A e^{-bu}\ ,$$

where $u=E/E_g$ and

$$\beta_u=[1-(2m_h/uE_g)^2]^{1/2}\ .$$

(2) The three gluons in upsilon decay hadronize independently. For a fixed gluon energy the hadron spectrum is independent of how many other gluons there are. We note, however, that this may not be a safe approximation; in many models[12,24,25] gluons do not fragment independently, and there is even some experimental evidence for this view.[26]

(3) The probability density G of gluon energies in $\Upsilon\to ggg$ decay is as given by QCD:[27]

$$G(v)=[2/(\pi^2-9)]\{v(1-v)/(2-v)^2+(2-v)/v+2[(1-v)/v^2-(1-v)^2/(2-v)^3]\ln(1-v)\} ,$$

where $v=2E_g/W$. This distribution is approximately linear, rising from $G(0)=0$ to $G(1)=2$.

In this picture the effect of the convolution of the gluon fragmentation function $D_g^h(E/E_g)$ with the gluon energy spectrum $G(2E_g/W)$ is to make the hadron spectrum in upsilon decays steeper than it would be if the upsilon had decayed into two fixed-energy gluons. That is, the upsilon spectrum should still be fit approximately by the βAe^{-bz} functional form, but with an effective slope parameter b larger (by about 1.6 units) than for a two-jet decay. The mean multiplicity of particles of mass m_h, which is just the integral of the z spectrum from $z_{\min}=2m_h/W$ to 1, is increased by $\frac{3}{2}$ in going from two jets to three, but this is compensated by the decreased multiplicities in lower-energy jets. This latter effect, which is well established for quark jets, comes, at least in part, from the nonscaling behavior of our assumed spectrum form in the vicinity of the z threshold, which is beam energy dependent ($z_{\min}=2m_h/W$). We extract the gluon fragmentation functions by finding the function $D_g^h(u)=\beta_u Ae^{-bu}$, which when convolved with the gluon energy distribution $G(z/u)$ gives the best fit to the observed hadron spectrum on the upsilon:

$$(1/N_\Upsilon)dn_\Upsilon^h/dz=3\int_z^1 D_g^h(u)G(z/u)du/u$$
$$=3\beta A\int_z^1 e^{-bu}G(z/u)du/u .$$

The A and b parameters for the quark and gluon fragmentation functions derived from our data are shown in Table VI. Also tabulated are the integrals, which since they are sensitive to the threshold $z_{\min}=m_h/E_{\text{jet}}$, are all computed assuming the same jet energy $M_\Upsilon/2$. We will discuss here the most accurately determined fragmentation functions, those for the charged pions, and postpone to the following sections the comparisons with other particles. The spectrum for pions falls off with increasing pion momentum more rapidly in upsilon decays than in the nonresonant data (Fig. 8 and Table V). This is only partially explained by the effect of the sharing of energy among the three gluons in the upsilon decay; that is, after accounting for this, the slope b_g of the unfolded gluon fragmentation function $D_g^h(z)$ (Table VI) is still somewhat steeper than the slope b_q of the quark function $D_q^h(z)$. The integrated mean number of charged pions in a gluon jet is also greater than that for a quark jet of the same energy. Since most charged particles produced are pions, the same inequality must hold for the overall mean charged multiplicity in gluon and quark fragmentation.

In the Lund string fragmentation picture[12] the quarks or gluons do not fragment independently and the increased multiplicity in three-gluon upsilon decay relative to $q\bar{q}$ hadronization at the same center-of-mass energy is a consequence of the greater length of the three color strings connecting the three primary gluons, relative to that of the single string connecting the q and $\bar{q}$.

C. Vector vs pseudoscalar mesons

Whether a meson is formed directly from a $q\bar{q}$ combination or is produced by the decay of a heavy unstable hadron, one expects spin one to be favored over spin zero by the statistics factor 3, multiplied by a suppression factor depending on masses. Since the vector mesons ρ,ω,ϕ,K^* are heavier than the pseudoscalar mesons π,η,η',K, any mass suppression will tend to make the vector/pseudoscalar ratio less than 3.

Since the K^*/K mass ratio (1.8) is closer to one than is the ρ/π mass ratio (5.6), we might expect to see a vector/pseudoscalar yield ratio near to the ideal 3/1. The integrated numbers of charged and neutral K^* per event (Table V) are 0.8 in the nonresonant continuum and 0.9 in upsilon decays, to be compared with K rates (charged and neutral) per event of 2.2 continuum and 2.4 upsilon. After subtraction, the rates for kaons not coming from K^* and ϕ are 1.2 both for continuum and upsilon; that is, about 50% higher than the K^* rates. In other words, the observed vector-pseudodscalar ratio for strange mesons is about 0.7 for 5-GeV quark jets and for gluon jets in upsilon decays. We can get an estimated total rate for vector mesons from four times the ρ^0 rate (to account for ρ^+, ρ^-, and ω), plus the K^* rates, plus the ϕ rates. This gives 2.3 per event in the continuum and 2.8 in upsilon decays.

It is noteworthy that all the vector mesons have considerably harder energy spectra (lower b) in the continuum, compared either with the continuum spectra of other particles or with the vector-meson spectra in upsilon decays.

D. Strange vs nonstrange

One can distinguish conceptually three sources of strange particles in upsilon or nonresonant e^+e^- final states (see Fig. 39).

(1) Strange particles made from the primary s and $\bar{s}$ quarks produced directly by the virtual photon:

$$e^+e^-\to\gamma\to s\bar{s}\to\text{strange hadrons}+\text{other hadrons} .$$

This mechanism does not occur in $\Upsilon\to ggg$ decays, but should occur in about $\frac{1}{10}$ of the nonresonant continuum events, accounting for two strange hadrons in each such event, or an average multiplicity of 0.2 strange particles per continuum event. The two hadrons of opposite strangeness will typically be leading particles in opposite jets, although the strong decays of excited strange particles can cause the observed "stable" strange particles to have nonleading momenta.

(2) Strange particles from the decay of primary c and $\bar{c}$ quarks:

$$e^+e^-\to\gamma\to c\bar{c}\to\text{charmed hadrons}+\text{other hadrons}$$
$$\to\text{strange hadrons}+\text{other hadrons} .$$

This should occur in $\frac{4}{10}$ of the continuum events, accounting for about 0.8 strange particles per event on average. The strange particles will be in opposite jets, but not

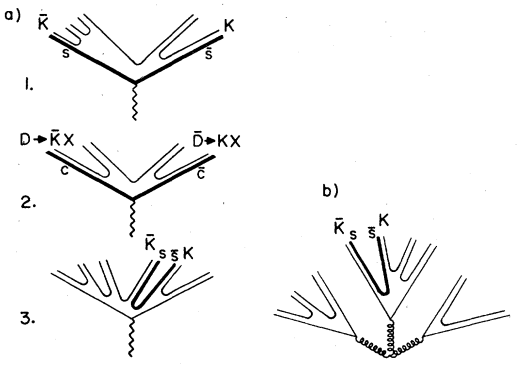

FIG. 39. Mechanisms of strange-particle production (a) in continuum e^+e^- annihilation and (b) in upsilon strong decay.

necessarily leading, and will have opposite strangeness. This process also does not occur in upsilon strong decays.

(3) Strange particles made from s and $\bar{s}$ quarks which materialize locally in pairs from the gluon field ("ocean"), either in the first step after the creation of the three primary gluons (in upsilon decay) or during the course of the hadronization process. They should occur in pairs of opposite strangeness, rather close in momentum space (within one or two units of rapidity). This mechanism should contribute both to continuum annihilation and to upsilon decay. One expects the production of $s\bar{s}$ pairs to be suppressed relative to $u\bar{u}$ or $d\bar{d}$ because of the higher mass; however, if the three primary gluons in upsilon decay are sufficiently far off the mass shell, the probability the $s\bar{s}$ creation in the earliest stage of the hadronization chain may not be suppressed. The creation of $c\bar{c}$ pairs from the gluon field is likely to be very strongly suppressed because of their greater mass.

Since the vector mesons have a narrower range of masses than do the pseudoscalar mesons and are also less likely to be products of the decay of heavier particles, we can see more clearly the effect of strangeness suppression in their production ratios. In an SU(3)-symmetric model we would expect ρ^0, K^*, ϕ production in the proportions 1:4:1. What we actually see (Table V) is 1:1.7:0.1 in the continuum and 1:1.6:0.3 in Υ decays. That is, mesons containing one (two) s quark(s) are suppressed by a factor of the order of $\frac{1}{3}$ ($\frac{1}{5}$) relative to SU(3) symmetry.

If we sum the integrated yields for charged and neutral kaons and for lambdas (with an arbitrary factor of two to account approximately for the other hyperons that we do not see), we can get an estimate of the mean number of strange particles per event. The result (Table V) turns out to be 2.3 (continuum) and 2.8 (upsilon) strange particles per event. On the average, each event has about one strange-particle pair.

The rates for the continuum are not surprising, and can easily be accommodated with 1.0 strange particles per event from primary s and c quarks [sources (1) and (2)] and the remaining 1.3 coming from the hadronization, with $s\bar{s}$ creation mass-suppressed to the level of about $\frac{1}{3}$ of the SU(3)-symmetric rate, $s\bar{s}=d\bar{d}=u\bar{u}$. This is confirmed by the Lund Monte Carlo calculation,[12] which gives good agreement with the data (including energy spectra) with an s/q (that is, s/u or s/d) hadronization ratio of about 0.3.

The results for the strong decays of the upsilon are not easily understood in an independent fragmentation picture. First, if we were to assume that gluons fragment like quarks, then the reduction in heavy hadron multiplicity per jet due to the three-gluon energy sharing would cause the expected mean multiplicity of strange particles from the upsilon to be less than in the continuum. We might expect it to be even lower, because sources (1) and (2) are not present in upsilon decay. Unfolding the gluon fragmentation function $D_g^K(z)$ from our measured upsilon decay spectrum and comparing the integral with that derived from our continuum quark fragmentation function D_q^K, we get 1.5 times as many strange particles in a 5-GeV gluon jet as in a 5-GeV quark jet. In the Lund Monte Carlo calculation[12] the higher kaon yield in upsilon decays comes out naturally, as a consequence of the greater number of quark pairs created in the three-gluon string configuration.

One might expect to see evidence for the contribution of leading kaons from primary $s\bar{s}$ or $c\bar{c}$ in the slope of the continuum kaon momentum spectrum, compared with the spectrum from upsilons. Actually, at our energies the Monte Carlo simulation of the fragmentation and decay cascade process (Fig. 40) shows that the kaons from the three mechanisms listed above lead to almost identical x spectrum shapes.

E. Baryons vs mesons

We can imagine baryons being produced in three ways (see Fig. 41).

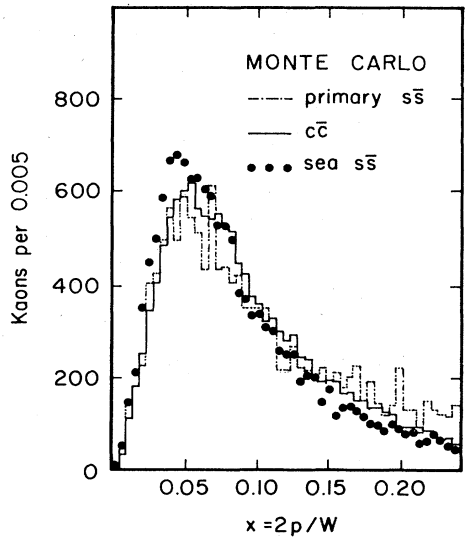

FIG. 40. Continuum kaon spectra predicted for the CLEO detector by a Lund Monte Carlo simulation (Ref. 12). The contributions of the three strange-quark production mechanisms (see Fig. 39) are separately plotted.

(1) Primary diquark pair production by the virtual photon:

$$e^+e^- \rightarrow \gamma \rightarrow qq + \bar{q}\bar{q} \rightarrow \text{baryon} + \text{antibaryon} + \text{mesons} .$$

This mechanism can contribute only to continuum production. The baryon and antibaryon should be leading particles in opposite jets. Relative to the pair production of pointlike quarks, diquark pair production would be suppressed by a form factor which should be small when the center-of-mass energy W is larger than the reciprocal of the radius r_{qq} of a diquark system. No one knows r_{qq}; it is usually expected to be of the order of 1 fm, although there are suggestions that it may be much smaller.[28] If r_{qq} is not small, then primary diquark pair production should be negligible at $W=10$ GeV.

(2) Diquark pairs created from the gluon field in the hadronization process. This could contribute to both upsilon and nonresonant baryon production. The baryon-antibaryon pair would be close in momentum space, in the same jet. One would expect the diquark pair production to be suppressed relative to quark pair creation, because of the higher mass.

(3) Baryons formed from recombination of triplets of quarks separately created. For example, the three primary gluons into which the upsilon first decays could each produce a $q\bar{q}$ pair, making three quarks and three antiquarks in the second generation of the fragmentation chain. These might then coalesce into a baryon and an antibaryon.[24,25,29]

Since our upsilon and continuum data samples were obtained from running at beam energies below the threshold for B meson production, the decay of B mesons to baryons[30] cannot contribute.

Since every hyperon decays eventually to a proton or neutron, we can estimate from our data the number of baryons produced per event by doubling the integrated rates for protons and antiprotons to account approximately for the undetected neutrons and antineutrons. The results (Table V) for the mean number per event are 0.8 (continuum) and 1.2 (upsilon). Note that two out of every three upsilon strong decays produce a baryon-antibaryon pair.[31]

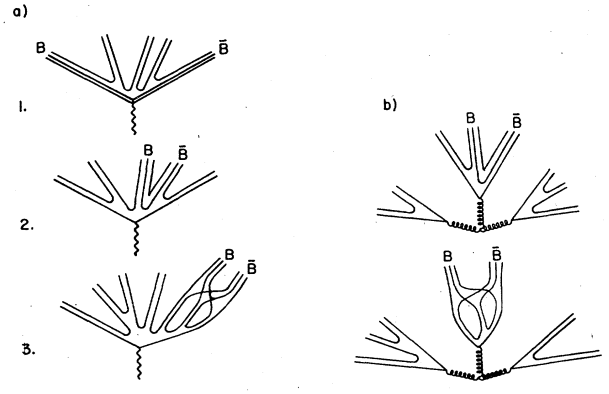

FIG. 41. Mechanisms of baryon production in (a) continuum e^+e^- annihilation and (b) in upsilon strong decay.

For continuum baryon production there are no *a priori* predictions to compare with. The observations, however, can be described quite well by the Lund Monte Carlo calculation,[12] which incorporates source (2) only, if one assumes a ratio $qq/q=0.07$ for the probability of diquark pair creation relative to quark-pair creation. The relative yields of proton, Λ, and Ξ can be adjusted by varying this ratio for the various diquark flavor combinations. It should be noted that in the context of the Lund model[12] the observation of Ξ production is direct evidence for the creation of strange diquark-antidiquark pairs.

If gluons fragmented independently with the same fragmentation functions as for quarks, one would expect the three-gluon energy sharing effect to cause a reduction in the number of baryons per event in upsilon decay. Instead, baryons are significantly more copious in upsilon decays than in the continuum (Table V). If we unfold the spectrum softening effect and compare gluon and quark fragmentation functions for proton production in fixed energy jets, the ratio of the integrals is 2.6 (Table VI). The effect is even greater for the lambda data, where the corresponding ratio is 6.2. This increase in baryon yields over naive expectations is probably the most striking difference between gluon fragmentation in upsilon decays and quark fragmentation in the continuum, and is a serious failing of the independent fragmentation models.[13,24] The Lund Monte Carlo simulation,[12] with the diquark/quark pair-creation ratio set at 0.07 to reproduce the continuum baryon yield, comes closer to accommodating our data on the upsilon. Apparently the three gluon string configuration provides more opportunities than the quark-antiquark string for diquark pair creation. It may be, as emphasized by Field,[26] that the baryon excess is due not to an intrinsic difference between gluon and quark jets, but to the fact that there are three jets instead of two.

IV. CORRELATIONS BETWEEN PARTICLE YIELDS AND GLOBAL EVENT CHARACTERISTICS

A. Event charged multiplicity

Figures 42(a) and 42(b) show the distribution of charged multiplicities for continuum annihilations and for upsilon direct decays, as observed in the CLEO detector. Since our purpose here is not to study the charged multiplicity distributions per se, but to note how they correlate with the presence of various particle species, we do not correct the distributions for detector acceptance and backgrounds. Such effects cause the observed mean multiplicity to be about one or two units less than the true mean multiplicity, but correcting the distributions introduces systematic errors because of uncertainties in the assumptions to be used in the simulations. The differences in acceptance between continuum and upsilon events is not enough to affect our conclusions.

The observed mean charged multiplicity for an upsilon strong decay is about one unit higher than for a continuum event. The 2.8 average observed multiplicity per gluon jet (one-third of the upsilon multiplicity) at an average energy of $M_\Upsilon/3=3.2$ GeV is about the same as the

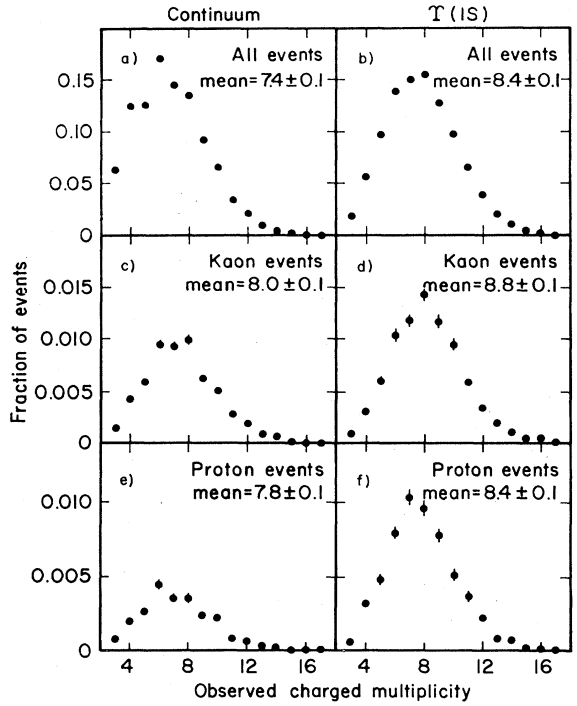

FIG. 42. Uncorrected observed charge multiplicity distributions for all (a) continuum and (b) upsilon events, and the corresponding distributions for events containing [(c) and (d)] a charged kaon, and [(e) and (f)] a proton or antiproton.

average multiplicity per quark jet as the same energy, estimated by extrapolating our two-jet continuum mean multiplicity from $W=10.5$ GeV down to 6.3 GeV assuming[32] a

$$3.33-0.80\ln W+1.04(\ln W)^2$$

dependence.

Figures 42(c) and 42(d) show the corresponding distributions for the events containing an identified charged kaon. The distributions are quite similar to those for all events. Actually, the mean observed charged multiplicity for kaon events is higher by 0.6 (0.4) for continuum (upsilon) data. Events containing identified p or $\bar{p}$ have multiplicities [Figs. 42(e) and 42(f)] increased by only 0.4 (0.0) for continuum (upsilon) data.

In Figs. 43(a) and 43(b) we show the dependence of the mean number of identified charged kaons per event on the charged multiplicity of the event. As one would naively expect, events with more charged particles have more kaons, with an almost linear relationship.

The corresponding situation for the protons (and antiprotons) is different. Although the mean number of identified p and $\bar{p}$ increases with the total charged multiplicity of the event [see Figs. 43(c) and 43(d)] up to multiplicity 6, it then saturates, and may even decrease at high event multiplicities. The larger proton rate in upsilon decays certainly cannot be explained just by the 14% excess in overall multiplicity relative to the continuum.

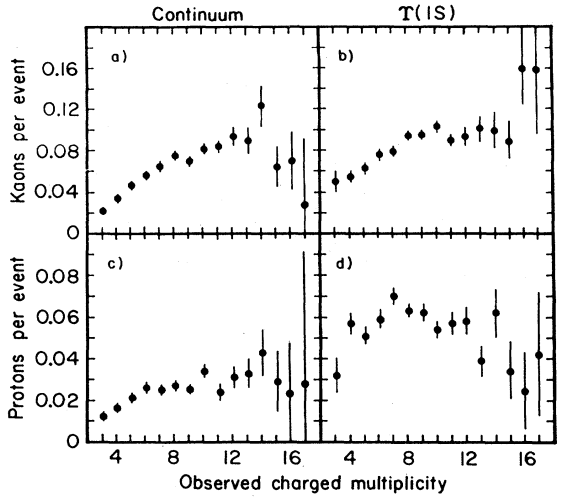

FIG. 43. Dependence of the average number of observed charged kaons [(a) and (b)] and protons (and antiprotons) [(c) and (d)] per event on the observed charged multiplicity of the event.

B. Event shapes

A convenient measure of the jettiness of an event, the tendency for the final-state momenta to align along an axis, is the ratio of Fox-Wolfram moments[10] $R_2=H_2/H_0$, essentially a normalized quadrupole moment of the event shape in momentum space. R_2 varies between 0 for a spherically symmetric topology and 1 for a completely aligned event.

As one would expect, continuum $q\bar{q}$ events have larger observed R_2 values [0.39 on average, at $W=10.4$ GeV, see Figs. 44(a) and 44(b)] than upsilon ggg events (0.19). The R_2 distributions for events containing identified kaons [Figs. 44(c) and 44(d)] and protons [Fig. 44(e) and 44(f)] are rather similar to the corresponding distributions for all events; the mean values are within 10% the same.

In the continuum the more jetlike events (with R_2 approaching 1) tend to have fewer kaons [Fig. 45(a)]. This may at least partially be a reflection of the fact that momentum conservation forces the very-low-multiplicity events to be aligned, and as we have already seen, low-multiplicity events contain fewer kaons. Also, continuum events in which the primary quarks are $c\bar{c}$ contain charmed particle decays, which make broader jets and contribute to the kaon yields. Such an effect is less obvious in upsilon decays [Fig. 44(b)]. Note though, that one cannot ascribe the higher p rates in upsilon decays (relative to continuum) to the lower average R_2 values in upsilon decays; even when compared at the same fixed R_2, the proton rates are higher in upsilon decays than in the continuum.

X. TWO-PARTICLE CORRELATIONS

A. Charge correlations

Overall charge is presumably conserved in every e^+e^- annihilation, but whether the positive and negative

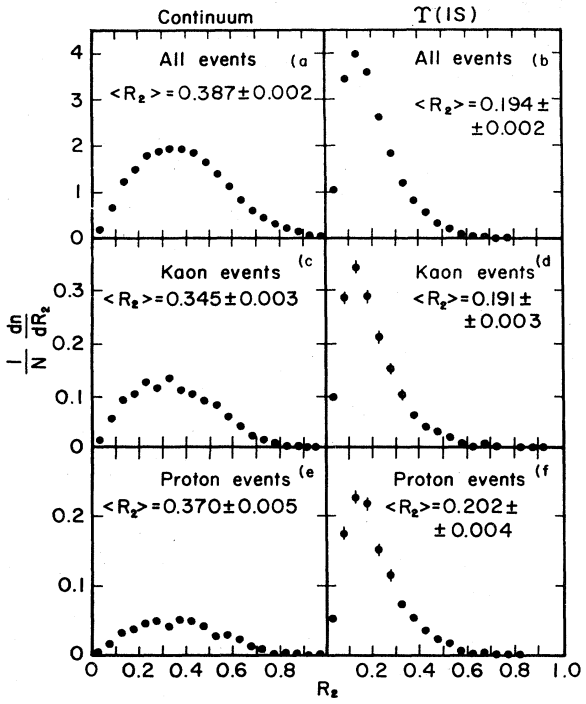

FIG. 44. Uncorrected distributions of the ratio R_2 of Fox-Wolfram moments (see text and Ref. 10) for all events in (a) the continuum and (b) upsilon decays, and the corresponding distributions for events containing [(c) and (d)] a charged kaon, and [(e) and (f)] a proton or antiproton.

charges in each event tend to be scattered randomly in momentum space or tend to pair up closely in momentum space (local compensation) or over longer intervals (long-range correlation) is sensitive to the production dynamics. Decaying resonances should produce short-range correlations, while the opposite charges of the primary $q\bar{q}$ pair in continuum annihilation should produce a long-range

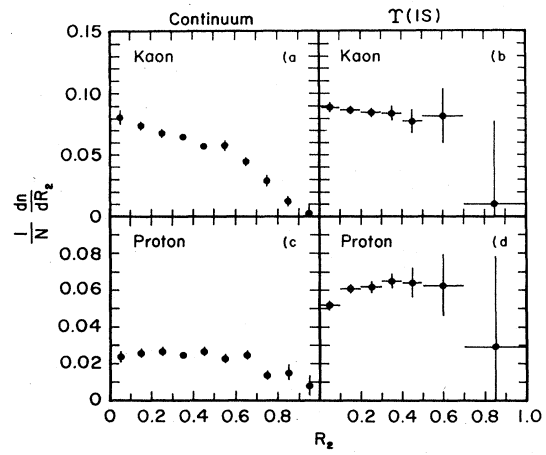

FIG. 45. Dependence of the average number of observed charged kaons [(a) and (b)] and protons (and antiprotons) [(c) and (d)] per event on the observed Fox-Wolfram ratio R_2 (see text and Ref. 10).

charge anticorrelation between leading hadrons in opposite jets. In any scheme of hadronization in which quark pairs are created from the neutral gluon field there will be a tendency toward short-range charge compensation.

Both short- and long-range correlations have been seen[33] in continuum data at center-of-mass energies above 30 GeV. In the usual analysis one determines the sphericity jet axis for each event, and for each charged hadron the rapidity y along the axis. For hadrons having rapidity magnitude y' (in a small interval $\Delta y'$, fixing the sign of the direction of the jet axis in each case so that y' is negative) one then plots the average charge of the other hadrons (plus for opposite sign, minus for same sign) as a function of their rapidity y. Although our kinematic range in rapidity is narrower, our continuum data (Fig. 46) show the same behavior as the measurements at higher incident energies.[33] That is, on the average, a leading hadron has its balancing charge peaked locally in the same jet (negative y) within two units of rapidity, but the distribution has a significant shoulder extending to positive y, corresponding to a long-range correlation in the opposite jet. This tendency for the leading back-to-back hadrons to be oppositely charged is evidence that the primary partons are oppositely charged.

It is interesting to look for the same effect in upsilon decays. Here the sphericity axis should approximate the direction of the most energetic of the three gluons. The data (Fig. 46) show the same peak at nearby rapidity, implying short-range charge compensation, but no shoulder at positive y. The charges of leading particles in widely separated jets are randomly correlated, implying that the primary partons in upsilon decay are neutral.

B. Data corrections

It is important in studying two-particle correlations to have an efficiency for particle detection and identification which covers a wide range of momenta. Otherwise, the observed correlations will tend to be dominated by spurious acceptance variations. Corrections for such effects are more difficult to make reliably in two-particle correlation data than in the case of single-particle measurements. For that reason most of the results in this section concern K^0K^0, $\Lambda\bar{\Lambda}$, and $K^0\Lambda$ (or $K^0\bar{\Lambda}$) correlations. The decay secondaries of neutral kaons and lambdas can be recognized with nearly uniform efficiency for all momenta above about 0.8 GeV/c.

We must correct the double vee signals for background events in which one or both of the vee candidates is an accidental combination of two charged tracks which happen to pass all requirements for the K^0 or Λ in question. We used a sideband subtraction scheme in which background double-vee data is generated from the mass sidebands of one vee combined with the sideband or signal of the other. We normalized this background double vee signal using the relative magnitudes of signal above background, of background, and of sidebands, which we got from a fit to the mass spectrum of each of the vees. The background is typically about 30% and the uncertainty in it contributes a 6% systematic error. Table VII lists the corrected number of double vees.

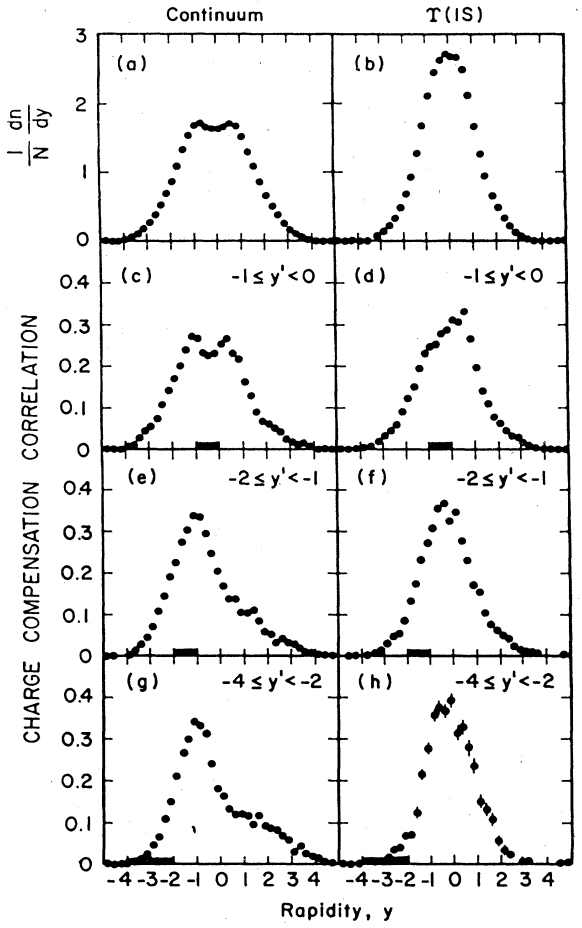

FIG. 46. (a) and (b) Uncorrected distribution of all observed charged particles in rapidity with respect to the sphericity-defined jet axis of the event, for continuum (a) and upsilon (b) data. The dip at zero rapidity in the continuum data is at least partly due to our inability to detect particles at very low momenta; it is filled-in in the upsilon data by the steeper momentum spectrum and the larger number of particles at higher p_T in the more spherical events. (c)—(h) Two-particle charge correlations: in each plot one particle is fixed at rapidity y' (which defines the negative rapidity direction and is indicated by a bar on the horizontal axis) and the density of all other particles in the same event is plotted, plus for opposite sign and minus for same sign.

We have already discussed in Sec. VI the calculation by Monte Carlo simulation of the efficiency for recognizing $K_S^0 \to \pi^+\pi^-$ and $\Lambda \to p\pi^-$ (and charge conjugate) decays. In order to get the two-particle acceptances, we did an abbreviated Monte Carlo calculation using the event generator and smoothed approximations to the single-vee efficiencies as functions of production momentum and angle. These two-particle acceptances are shown as the curves in Figs. 47, 49, and 50. They include the effects of vee reconstruction efficiency, undetectable momenta, geometrical aperture, and unseen decay modes ($K_S^0 \to \pi^0\pi^0$, $K_L \to$ anything, and $\Lambda \to n\pi^0$).

The K^+, K^-, p, and $\bar{p}$ pair rates listed in Table VII were corrected for acceptance simply by dividing by the appropriate single-particle acceptances. The single-particle acceptances used were just the ratios of observed single-particle rate to corrected mean number per event ($\bar{n}$ in Table V).

TABLE VII. Measured pair rates, corrected for acceptance.

Pair	Continuum observed	Corrected rate/event	Upsilon observed	Corrected rate/event
K^+K^+	27	0.13±0.03	37.7	0.18±0.03
K^-K^-	17	0.10±0.03	27.4	0.17±0.04
K^+K_S	89	0.27±0.03	109.0	0.39±0.04
K^-K_S	84	0.28±0.03	89.3	0.39±0.05
K_SK_S	193	0.24±0.03	293.0	0.52±0.05
K^+K^-	76	0.41±0.05	125.5	0.69±0.07
$K_S(\Lambda$ or $\bar{\Lambda})$	45	0.07±0.01	94.3	0.15±0.02
pp or $\bar{p}\bar{p}$	10	0.0178±0.005	14.2	0.024±0.007
$p\bar{p}$	37	0.06±0.01	73.5	0.11±0.02
$\Lambda\Lambda$ or $\bar{\Lambda}\bar{\Lambda}$	0	0±0.003	0	0±0.02
$\Lambda\bar{\Lambda}$	10	0.016±0.005	16.2	0.03±0.9
$p\Lambda$ or $\bar{p}\bar{\Lambda}$	2	0.004±0.003	6.4	0.04±0.02
$p\bar{\Lambda}$ or $\bar{p}\Lambda$	17	0.04±0.01	42.1	0.25±0.04

C. *KK* correlations

As expected, the kaon pair rates show evidence of strangeness conservation. The K^+K^- and $K_S^0K_S^0$ pair rates (Table VII), both in the continuum and in upsilon

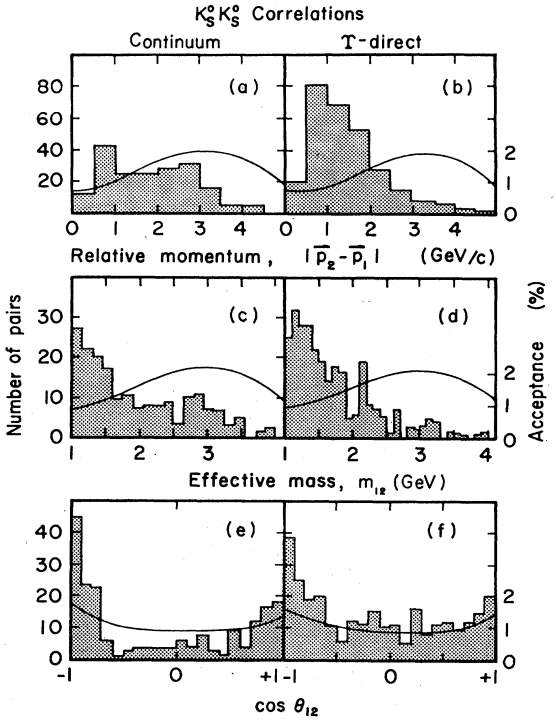

FIG. 47. Observed $K_S^0K_S^0$ correlations for continuum data and upsilon strong decays, plotted in terms of [(a) and (b)] the relative momentum $|\mathbf{p}_1 - \mathbf{p}_2|$, [(c) and (d)] the effective mass m_{12}, and [(e) and (f)] the cosine of the angle θ_{12} between the two momenta. The curves show the estimated acceptance.

decays, are similar to the K^+ and K_S^0 inclusive rates (Table V rates divided by two), while the rates for like-charge pairs are much smaller.

One way to look for evidence of the several possible mechanisms for strange-particle production discussed in Sec. VII C is to examine the kaon pair momentum correlations. A primary $s\bar{s}$ pair created by the virtual photon in continuum e^+e^- annihilation should produce leading kaons in opposite jets widely separated in momentum; later $s\bar{s}$ pairs from the gluon field should produce local kaon pairs; while decay of charmed particles from primary $c\bar{c}$ quarks should be intermediate.

Figures 47(a) and 47(b) shows the distributions in relative momentum for K_S^0 pairs observed in the continuum and in upsilon strong decays. The data are not corrected for acceptance, but the estimated acceptance is plotted as a separate curve. In spite of the fact that the latter peaks at 3-GeV/c relative momentum, the observed pairs are concentrated much lower. This is not surprising in view of the steep falloff in the single-particle momentum spectrum. There is a hint of the contribution of primary $s\bar{s}$ or $c\bar{c}$ in the continuum showing as a slightly broader relative momentum spectrum, compared to that for upsilon decays. The same behavior is evident in the plots of pair invariant masses [Figs. 47(c) and 47(d)].

The distribution in the cosine of the angle between the two kaon momenta [Figs. 47(e) and 47(f)] shows a preference for back-to-back production ($\cos\theta_{12} = -1$), especially strong in the continuum data. Before interpreting this as convincing evidence for primary $s\bar{s}$ or $c\bar{c}$ contribution, we should remember first that most of the pairs are separated by rather low relative momenta, and second that the rarer high momentum kaons come in low multiplicity events and tend to bias their partners in favor of opposite production directions to conserve overall momentum. Nevertheless, the contrast between the upsilon and continuum $\cos\theta_{12}$ distributions does argue for a primary $s\bar{s}$ and $c\bar{c}$ contribution to the continuum data. Figure 48 shows the corresponding $\cos\theta_{12}$ plot for K^+K^- pairs, in which the kaons are confined to the momentum range (0.5 to 1.0 GeV/c) within which we can identify them. The upsilon data show a greater tendency for the K^+K^- to be in the same jet, relative to the continuum data.

D. $\Lambda\bar{\Lambda}$ and $K\Lambda$ correlations

The effect of strangeness and baryon number conservation can be seen in the fact that the $\Lambda\bar{\Lambda}$ pair rates (Table VII) are consistent, within wide errors, with the inclusive Λ rates (Table V rates divided by two).

The distributions in $\cos\theta_{12}$, $|\mathbf{p}_2 - \mathbf{p}_1|$, and m_{12} for $\Lambda\bar{\Lambda}$ pairs (Fig. 49) and $K\Lambda$ pairs (Fig. 50) are qualitatively similar to those seen in the case of KK pairs, but because of the smaller number of hyperons, the statistical significance is weaker. There seems however to be an increase in the momentum difference (and effective mass) for $\Lambda\bar{\Lambda}$ pairs in upsilon decays: an average $|\mathbf{p}_2 - \mathbf{p}_1|$ of 2.0 GeV/c, to be compared with about 1.3 GeV/c for KK and $K\Lambda$ pairs from the upsilon and about 1.5 GeV/c for KK, $K\Lambda$, and $\Lambda\bar{\Lambda}$ pairs in the continuum. There is also a stronger back-to-back peaking in the $\cos\theta_{12}$ plot for $\Lambda\bar{\Lambda}$

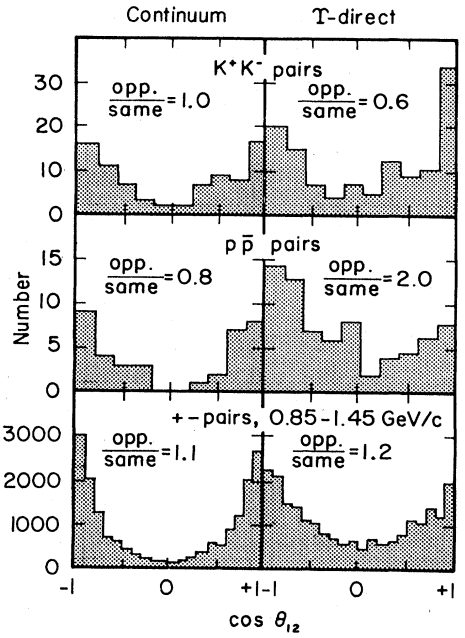

FIG. 48. Distribution in the cosine of the angle θ_{12} between particle and antiparticle momenta for K^+ and K^- (top row), for proton and antiproton (middle), and for all charged particles whose momenta are within the range in which protons are identified (bottom row). The ratios of numbers of pairs with negative and positive $\cos\theta_{12}$ are indicated.

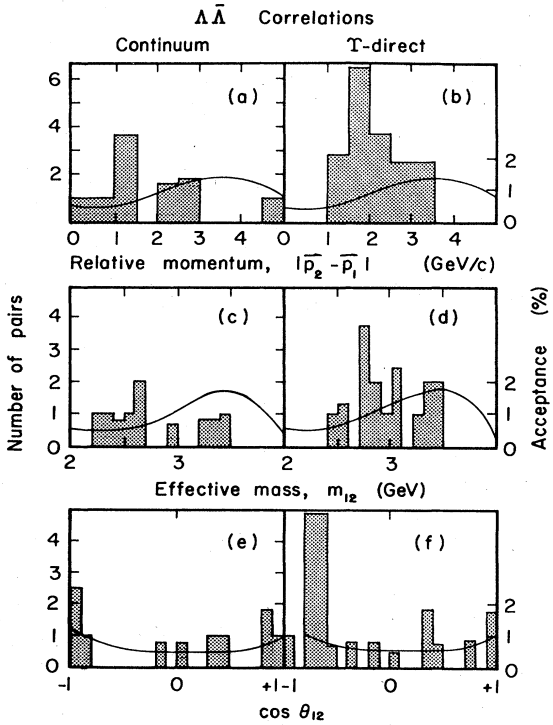

FIG. 49. Observed $\Lambda\bar{\Lambda}$ correlations for continuum data and upsilon strong decays, plotted in terms of [(a) and (b)] the relative momentum $|\mathbf{p}_1 - \mathbf{p}_2|$, [(c) and (d)] the effective mass m_{12}, and [(e) and (f)] the cosine of the angle θ_{12} between the two momenta. The curves show the estimated acceptance.

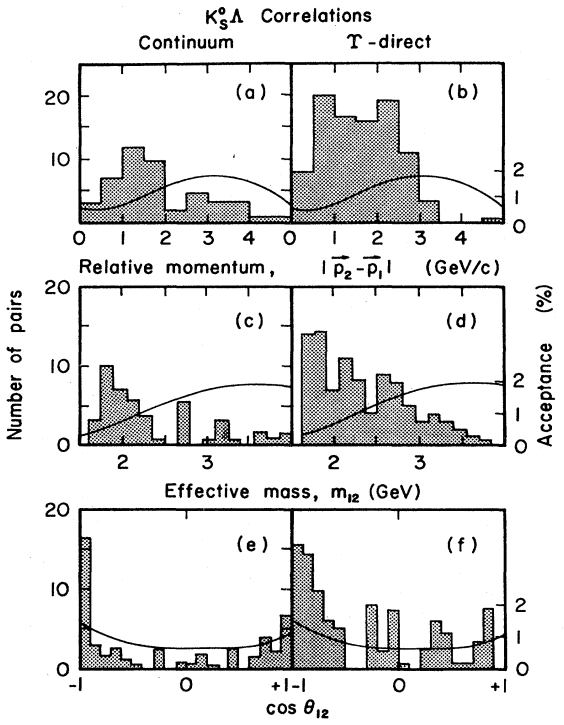

FIG. 50. Observed $K^0_S\Lambda$ correlations for continuum data and upsilon strong decays, plotted in terms of [(a) and (b)] the relative momentum $|\mathbf{p}_1-\mathbf{p}_2|$, [(c) and (d)] the effective mass m_{12}, and [(e) and (f)] the cosine of the angle θ_{12} between the two momenta. The curves show the estimated acceptance.

from the upsilon than for any of the other cases. This can also be seen in the $\cos\theta_{12}$ plots for identified proton-antiproton pairs (Fig. 48); the ratio of opposite hemisphere to same hemisphere is 2.0 in upsilon decays compared to 0.8 in the continuum. The corresponding ratios are 1.0 and 1.1 for all oppositely charged particles with momenta in the range 0.65 to 1.35 GeV/c (our proton identification range). That is, while baryon-antibaryon correlations are mainly at short range in continuum e^+e^- annihilation,[34] our data suggest that in the three-gluon decay of the upsilon, baryon and antibaryon may have long-range correlations and may even be leading particles in different jets.

XI. CONCLUSIONS

Inclusive hadron production rates, energy spectra, and correlations in continuum e^+e^- annihilation have been studied in previous experiments over a wide center-of-mass energy range.[15,17,18,20,22,33,34] Many features have been observed: mean multiplicities of various particle species, quark fragmentation functions, the scaling of the single-particle distributions with respect to the incident energy, long- and short-range correlations, and jet topologies. In our inclusive studies of upsilon strong decays we have observed that many characteristics of the upsilon final states repeat the observations of nonresonant continuum final states; for example, the ratio of charged- and neutral-pion rates, and short-range charge correlations in charge, strange particles, and baryon-antibaryon pairs. There are, however, significant differences observed.

(1) The rate of falloff of the single-particle spectra with increasing x (that is $2p/W$) or increasing z ($=2E/W$) is generally faster for upsilon decays than for continuum annihilations. Much of this effect can be attributed to the sharing of the available energy among three jets instead of two, but even after unfolding the assumed QCD gluon-energy distribution, the derived gluon fragmentation functions $D_g^h(z)$ are typically steeper than the corresponding quark fragmentation functions $D_q^h(z)$ derived from our continuum data.

(2) The production of heavier particles in upsilon decays is not suppressed as strongly as in continuum events, and the contrast becomes more striking the heavier the particle (see Fig. 51). If partons fragmented independently, we would expect to see fewer heavy particles in upsilon decays. First, the heavier quarks can be pair produced by the original virtual photon in continuum annihilation without mass suppression, but such a mechanism is presumably absent in the three-gluon decay of the upsilon. And second, the fact that the average energy, $M_\Upsilon/3=3.2$ GeV, of each of the three primary gluons is less than the energy of a continuum primary quark (5.2 GeV at the $W=10.4$-GeV c.m. energy of our data) should make the production of massive particles more difficult. Two-thirds of all upsilon strong decays have a baryon-antibaryon pair.

(3) There is no long-range anticorrelation in particle charge in upsilon decays as there is in the continuum data, indicating that the primary partons (gluons) in upsilon decays are neutral. There is, however, evidence for a long-range contribution to the baryon-antibaryon correlation, as shown in the relative momentum and angle distributions.

The second and third observations may lead one to speculate that in some upsilon decays one or several of the

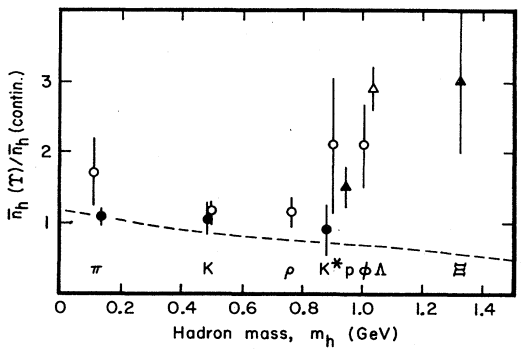

FIG. 51. For each hadron species h, the measured ratio of upsilon and continuum yields (mean number of h per event) as a function of the mass m_h. Open circles (mesons) and triangles (baryons) represent neutral-hadron ratios; closed symbols represent charged ratios. In an independent-fragmentation model in which gluons fragment like quarks, the ratios would follow the dashed curve.

three gluons are far off the mass shell. Heavy-particle states may not be strongly suppressed in the hadronization of such off-mass-shell gluons. For example, if such a gluon has large energy and small three-momentum, it can create a pair of diquarks with high opposite momenta, eventually resulting in leading back-to-back baryon and antibaryon. Or if the three gluons all have small three-momenta, they can produce three back-to-back energetic quark-antiquark pairs, which if the directions are parallel, may coalesce into a baryon and an antibaryon with large, oppositely directed momenta.

ACKNOWLEDGMENT

This work was supported in part by the National Science Foundation and the U.S. Department of Energy.

*Present address: University of Oklahoma, Norman, OK 73019.
†Present address: Indiana University, Bloomington, IN 47405.
‡Present address: Texas Accelerator Center, The Woodlands, TX 77380.

[1]T. Appelquist and H. Politzer, Phys. Rev. Lett. **34**, 43 (1980); Phys. Rev. D **12**, 1404 (1975).
[2]C. Berger *et al.*, Phys. Lett. **78B**, 176 (1978); Z. Phys. C **8**, 101 (1981); R. Cabenda, thesis, Cornell University, 1982.
[3]See, for example, the review of G. Wolf, in *Proceedings of the 21st International Conference on High Energy Physics, Paris, 1982,* edited by P. Petiau and M. Porneuf [J. Phys. (Paris) Colloq. **43**, C3-525 (1982)].
[4]P. Avery *et al.*, Phys. Rev. Lett. **51**, 1139 (1983).
[5]D. Besson *et al.*, Phys. Rev. Lett. **54**, 381 (1985).
[6]See, for example, the review by P. M. Tuts, in *Proceedings of the 1983 International Symposium on Lepton and Photon Interactions at High Energies,* Ithaca, New York, edited by D. G. Cassel and D. L. Kreinick (Newman Laboratory of Nuclear Studies, Cornell University, Ithaca, 1984), p. 284.
[7]D. Andrews *et al.*, Nucl. Instrum. Methods **211**, 47 (1983).
[8]R. Ehrlich *et al.*, Nucl. Instrum. Methods **211**, 17 (1983).
[9]R. Giles *et al.*, Phys. Rev. D **29**, 1285 (1984).
[10]G. C. Fox and S. Wolfram, Phys. Rev. Lett. **41**, 1581 (1978).
[11]C. A. Blocker *et al.*, Phys. Rev. Lett. **49**, 1369 (1982).
[12]B. Andersson, G. Gustafson, G. Ingelman, and T. Sjostrand, Phys. Rep. **97**, 31 (1983) and earlier papers listed therein; T. Sjostrand, Comp. Sci. Comm. **27**, 243 (1982); **28**, 229 (1983).
[13]R. D. Field and R. P. Feynman, Phys. Rev. D **15**, 2590 (1977); Nucl. Phys. **B136**, 1 (1978).
[14]D. Andrews *et al.*, Phys. Rev. Lett. **50**, 807 (1983); D. Besson *et al.*, Phys. Rev. D **30**, 1433 (1984).
[15]D. G. Aschman *et al.*, Phys. Rev. Lett. **41**, 445 (1978); R. Brandelik *et al.*, Nucl. Phys. **B148**, 189 (1979); Phys. Lett. **94B**, 444 (1980); **113B**, 98 (1982); M. Althoff *et al.*, Z. Phys. C **17**, 5 (1983); W. Bartel *et al.*, *ibid.* **20**, 187 (1983); H. Aihara *et al.*, Phys. Rev. Lett. **52**, 577 (1984).
[16]See the review by D. Sivers, Ann. Rev. Nucl. Part. Sci. **32**, 149 (1982), and other references cited therein.
[17]D. L. Scharre *et al.*, Phys. Rev. Lett. **41**, 1005 (1978); R. Brandelik *et al.*, Phys. Lett. **108B**, 71 (1982); H. J. Behrend *et al.*, Z. Phys. C **14**, 189 (1982); **20**, 207 (1983).
[18]V. Luth *et al.*, Phys. Lett. **70B**, 120 (1977); R. Brandelik *et al.*, *ibid.* **94B**, 91 (1980); **105B**, 75 (1981); C. Berger *et al.*, *ibid.* **104B**, 79 (1981); W. Bartel *et al.*, *ibid.* **104B**, 325 (1981); M. Althoff *et al.*, *ibid.* **130B**, 340 (1983).
[19]B. Andersson, G. Gustafson, and G. Ingelman, Phys. Lett. **85B**, 417 (1979); B. Andersson, G. Gustafson, and T. Sjostrand, Nucl. Phys. **B197**, 45 (1982).
[20]R. Brandelik *et al.*, Phys. Lett. **117B**, 135 (1982).
[21]Particle Data Group, Phys. Lett. **111B**, 1 (1982).
[22]H. Aihara *et al.*, Phys. Rev. Lett. **52**, 2201 (1984).
[23]P. Hoyer *et al.*, Nucl. Phys. **B161**, 349 (1979); A. Ali *et al.*, Phys. Lett. **93B**, 155 (1980); Nucl. Phys. **B167**, 454 (1980).
[24]R. D. Field and S. Wolfram, Nucl. Phys. **B213**, 65 (1983); R. D. Field, Phys. Lett. **135B**, 203 (1984); B. R. Webber, Nucl. Phys. **B238**, 492 (1984); T. D. Gottschalk, *ibid.* **B214**, 201 (1983).
[25]A. Snyder and C. G. Trahern, Phys. Lett. **129B**, 117 (1983).
[26]W. Bartel *et al.*, Z. Phys. C **21**, 37 (1983).
[27]K. Koller and T. F. Walsh, Nucl. Phys. **B140**, 449 (1978); H. Fritzsch and K.-H. Streng, Phys. Lett. **74B**, 90 (1978).
[28]M. Pavkovic, Phys. Rev. D **14**, 3186 (1976); K. T. Chao, Z. Phys. C **7**, 317 (1981); S. Fredriksson, M. Jandel, and T. Larsson, *ibid.* **14**, 35 (1982); **19**, 53 (1982); T. Meyer, *ibid.* **12**, 77 (1982).
[29]A. Casher, H. Neuberger, and S. Nussinov, Phys. Rev. D **20**, 179 (1979).
[30]M. S. Alam *et al.*, Phys. Rev. Lett. **51**, 1143 (1983).
[31]The excess of baryons on the $\Upsilon(1S)$ was first reported by C. W. Darden *et al.*, Phys. Lett. **80B**, 419 (1979).
[32]M. Althoff *et al.*, Z. Phys. C **22**, 307 (1984).
[33]R. Brandelik *et al.*, Phys. Lett. **100B**, 357 (1981).
[34]M. Althoff *et al.*, Phys. Lett. **139B**, 126 (1984).